DISSERTATIONS IN
FORESTRY AND
NATURAL SCIENCES

Nina Rogelj

Goniospectrometric analysis of optically complex samples

A study of diffraction gratings, optically variable devices, and coatings with special effect pigments

Publications of the University of Eastern Finland
Dissertations in Forestry and Natural Sciences No 203

UNIVERSITY OF
EASTERN FINLAND

NINA ROGELJ

Goniospectrometric analysis of optically complex samples

A study of diffraction gratings, optically variable devices, and coatings with special effect pigments

Publications of the University of Eastern Finland
Dissertations in Forestry and Natural Sciences
No 203

Academic Dissertation
To be presented by permission of the Faculty of Science and Forestry for public examination in the Auditorium AU100 in Aurora Building at the University of Eastern Finland, Joensuu, on December, 8, 2015,
at 12 o'clock noon.

Department of Physics and Mathematics

Printing:
Grano Oy
Jyväskylä, 2015

Editors:
Prof. Pertti Pasanen, Prof. Kai Peiponen
Prof. Pekka Kilpeläinen, Prof. Matti Vornanen

Distribution:
University of Eastern Finland Library / Sales of publications
julkaisumyynti@uef.fi
http://www.uef.fi/kirjasto

ISBN: 978-952-61-1986-1 (printed)
ISSNL: 1798-5668
ISSN: 1798-5668
ISBN: 978-952-61-1987-8 (pdf)
ISSNL: 1798-5668
ISSN: 1798-5676

Author’s address:
University of Eastern Finland
Institute of Photonics
P.O. Box 111
80101 Joensuu
FINLAND
email: nina.rogelj@uef.fi

Supervisors:
Markku Hauta-Kasari, Ph.D.
University of Eastern Finland
Institute of Photonics
P.O. Box 111
80101 Joensuu
FINLAND
email: markku.hauta-kasari@uef.fi

Marta Klanjšek Gunde, Ph.D.
National Institute of Chemistry
Laboratory for Materials Chemistry
Hajdrihova 19
1000 Ljubljana
SLOVENIA
email: marta.k.gunde@ki.si

Reviewers:
Francisco Miguel Martínez Verdú, Ph.D.
University of Alicante
Department of Optics, Pharmacology and Anatomy
Ap. de Correos, 99
03080 Alicante
SPAIN
email: verdu@ua.es

Frédéric Leloup , Ph.D.
Light & Lighting Laboratory
KU Leuven, Technology Campus Ghent
Gebroeders De Smetstraat 1
9000 Ghent
BELGIUM
email: frederic.leloup@kuleuven.be

Opponent:
Thomas A. Germer, Ph.D.
The National Institute of Standards and Technology
Sensor Science Division
100 Bureau Drive
20899-1070 Gaithersburg, Maryland
USA
email: thomas.germer@nist.gov

ABSTRACT

Many applications use gonioapparent targets whose appearance depends on illumination and viewing angles. Security and authentication applications use optically variable devices, while coatings with special effect pigments are used in automotive, decorative and security coatings. This study focuses on how to characterize these gonioapparent targets in a simple and effective way.

One of the methods for the characterization of such targets is the so-called ″digital numerical analysis″ (DNA), which transforms the bidirectional reflectance distribution function (BRDF) to goniospectrometric space. This is done via the summation of spatially undersampled BRDF over all directions and repeating this for all wavelengths in the visible spectral range, which results in a 3D goniospectrometric space curve (also called xDNA curve). The characterization capability of goniospectrometric space curves is first tested with a commercial multi-angle spectrometer having two illumination angles (45° and 15°) and 19 measurement angles (11 in-plane and 8 off-plane angles). The goniospectrometric space curve enables distinguishing between samples of different roughnesses, an interference effect on various transparent layers, and selective spectral absorption of light in differently thick pigmented coatings. Based on these results, systematic analysis of the goniospectrometric space curve is performed for optically complex samples; diffraction gratings, optically variable devices and coatings with special effect pigments.

The BRDFs of the diffraction gratings are calculated by applying diffraction theory and then transformed into goniospectrometric space using 6 in-plane angles and a 45° illumination angle. Gratings with parallel sinusoidal grooves having periods of 0.3–5.0 μm and amplitudes below 0.2 μm are analyzed. Goniospectrometric space curves of diffraction gratings consist of lines with different slopes and possible interconnections. The length of the xDNA curve is directly connected to the grating period and the amplitude, and the slope only to the former grating parameter.

The question regarding the angular and spectral resolution needed for a goniospectrometric space curve is addressed by building a bidirectional spectrometer capable of measuring all azimuthal angles and polar angles up to 60°, with a 2° step in both directions. The bidirectional spectrometer is used to measure the full BRDFs of diffraction gratings and optically variable devices, which are then converted into goniospectrometric space. This study finds that the goniospectrometric space curve performs adequately even with a reduced spectral resolution of 10 nm. Furthermore, it finds that the xDNA curve works best with ten measurement geometries, since oversampling in the angular sense reduces the uniqueness of the sample-specific goniospectrometric space curve.

Coatings with special effect pigments having specific parameters needed for a systematic research are hard to prepare. Thus, a numerical model for goniometric reflectance of these coatings is developed. Parameters, such as different types of pigments, surface coverage of pigments, pigment orientation distribution and the coating's substrate, are varied and the change in the reflectance spectra is evaluated. Afterwards, spectra are transformed into a goniospectrometric space curve and the obtained curve is analyzed while varying the previously mentioned parameters. It is found that the shape, position and orientation of the goniospectrometric space curve reveal the optical makeup of the coating.

This study confirms that the goniospectrometric space curve can be regarded as an appearance fingerprint of optically complex samples. Furthermore, it can be used with commercial hand held multi-angle spectrometers that have reduced spectral resolution (10 nm wavelength step) and small amounts of measurement geometries. It is shown that measurement geometry using 10 reflected angles (6 in-plane and 4 off-plane) at a 45° illumination angle is suitable to obtain a unique goniospectrometric space curve, that truly characterizes the measured sample.

Universal Decimal Classification: -046.44, 52-355, 52-652, 535.36, 535.4, 535.42, 535.421, 535.443, 535.662.1, 543.421/.424, 543.42, 543.424.4, 620.179.118, 620.198, 627.715.32, 667.633, 667.633.42, 676.017.55, 681.7.063

Library of Congress Subject Headings: Reflectance; Surface roughness–Measurement; Color; Optical spectroscopy; Materials–Appearance; Scattering (Physics); Spectrum analysis; Coatings; Diffraction; Diffraction gratings; Diffractive scattering; Optical spectrometers; Surfaces–Optical properties; Optical properties; Geometrical diffraction

Preface

First and foremost I would like to thank my mentor and supervisor Marta Klanjšek Gunde. You introduced me to the wonderful world of colors in science. You have stood beside me on my scientific path since the first page of the book that introduced us.

I would also like to thank my Finish supervisor Markku Hauta-Kasari, who gave me an opportunity to work in the Spectral Color Research Group and who guided me through all the formalities of obtaining a PhD.

A thank you also to the people working in the Spectral Color Research Group. Especially to Niko Penttinen - the goniometric measurements would not be possible without you.

Last, but not least, a big thank you to my family; my mom and my brother. This wonderful journey would not be possible without your love and support. Also, an enormous thank you to Domen. Thank you for being excited about all my pretty pictures, for traveling with me around Europe and for always pushing me to be a better person.

in Joensuu, November 15, 2015
Nina Rogelj

”There are two ways to live:
you can live as if nothing is a miracle;
you can live as if everything is a miracle.”
- *Albert Einstein*

LIST OF PUBLICATIONS

This thesis consists of the present review of the author's work in the field of the optical properties of gonioapparent samples and the following selection of the author's publications:

I M. Klanjšek Gunde and N. Rogelj, "Suitability of goniospectrophotometric space curves as appearance fingerprints," *Applied Optics* **52,** 2718-2728 (2013).

II N. Rogelj, I. Poberaj and M. Klanjšek Gunde, "Goniospectrophotometric space curves of diffraction gratings and their applicability as appearance fingerprints," *Applied Optics* **52,** 8355-8362 (2013).

III N. Rogelj, N. Penttinen and M. Klanjšek Gunde, "Evaluation of complex gonioapparent samples using a bidirectional spectrometer," *Optics Express* **23,** 22004-22011 (2015).

IV N. Rogelj, N. Penttinen, M. Čekada and M. Klanjšek Gunde, "Goniospectrometric space: Identifiable presentation of spectral goniometric data for complex diffractive samples," *Applied Optics* (**Submitted**).

V N. Rogelj and M. Klanjšek Gunde, "Modelling reflectance factor for special effect pigment coatings," *Journal of print and media technology research* **4** (2015).

VI N. Rogelj and M. Klanjšek Gunde, "Goniospectrometric space curve for special effect coatings," *Applied Optics* (**Submitted**).

Throughout the thesis, these papers will be referred to by Roman numerals given above. The papers have been included at the end of this thesis with the permission of the copyright holders.

AUTHOR'S CONTRIBUTION

The publications selected in this dissertation are original research papers, and the contributions of the authors are summarized as follows.

The idea for Paper **I** was originated by the lead author Marta Klanjšek Gunde and all the measurements were performed by the co-author Nina Rogelj. The results were analyzed by both authors; the manuscript was written by the lead author with the help of co-author.

Paper **II** uses numerical computations that were performed by the lead-author. The idea for it arose from discussions between the authors. The results were analyzed by all authors and the manuscript was written as a collaboration between the lead author and co-author Marta Klanjšek Gunde.

The idea for Paper **III** was originated from discussions between the authors. The bidirectional spectrometer was rebuilt and programmed by Niko Penttinen, Ph.D.; testing measurements were performed as a collaboration between Niko Penttinen, Ph.D. and the lead author. Sample measurements and numerical computations were done by the lead author and analyzed by all authors. The manuscript was written by the lead author in collaboration with the co-authors.

Discussions between the lead author and co-author Marta Klanjšek Gunde lead to the idea of Paper **IV**. Sample measurements with a bidirectional spectrometer as well as numerical computations were performed by the lead author, optical microscope measurements of the OVD samples were done by the co-author Miha Čekada. The results were analyzed mostly by lead author and co-author Marta Klanjšek Gunde, with the help of co-author Niko Penttinen. The manuscript was written by the lead author in collaboration with co-authors.

The idea for Papers **V** and **VI** arose from discussions between the two authors. The development of the numerical model and all numerical computations were performed by the lead author; the results were then analyzed by both authors. Manuscripts for Papers **V** and **VI** were written by the lead author in collaboration with the co-author.

Contents

1 Introduction

Surfaces that change their appearance significantly with illumination and viewing directions are becoming increasingly important in several applications, ranging from the purely decorative up to various functional and security purposes. The unique optical impressions of optically complex surfaces provide eye-catching effects, such as angle-dependent interference colors, pearl lustre, multiple reflection and depth illusion, which are characteristic of the gonioapparent effect. A large variety of samples fall into this class, giving angle-dependent effects due to

- surface effects originating in the topography of the micro- and macro textures of surfaces, such as leather, textile and other microtextured surfaces, including diffractive samples, and
- volume effects/optical effects coming from the inside of samples, caused by metallic, transparent, layered and surface-structured flaky pigments (so-called special effect pigments) applied in coatings, plastics and printing inks, which are mostly used in automotive, decorative and security coatings.

The optical properties of gonioapparent samples range well beyond solid color and cannot be described by any straightforward colorimetric measurement. While advanced applications are becoming more and more important, the appearance of such objects must be described precisely, and produced in a predictable and controllable way. This requires several conditions to be met, among them is the possibility to predict the angular dependent appearance, to measure it with different levels of precision, and to document it in a convenient way. A suitable evaluation metrics would be beneficial for the comparison of similar samples.

The complexity of gonioapparent properties is best described by the bidirectional reflectance distribution function (BRDF). It is defined as the ratio between the radiance reflected from a surface element into a unit solid angle, and the incident irradiance on the same surface element, for all possible illumination and viewing directions [1, 2]. It can be measured by a bidirectional spectrometer, an instrument with movable source of collimated light and movable detector. In practice, the light reflected in many directions over the entire hemisphere is measured for some selected illumination angles. Such devices are capable of providing data for standards and reference measurements [3–7].

The concept of BRDF was applied to describe the gloss of painted samples [8], and to represent the measurements in the CIE 1976 color space (CIELAB), defined by the Commission Internationale de l'Eclairage (CIE) [9]. Three-dimensional appearance characterization showed that the standard reflection materials are non-Lambertian reflectors at large illumination angles [10, 11]. Systematic study has shown that the curvature of the BRDF as a function of the viewing angle of four common diffuse reflectance standards changes with the illumination angle, but the variation is not the same for all the standards [11]. This confirms that a perfectly reflecting diffuser cannot be realized; moreover, the strong deviations from the properties of an ideal diffuser lead to large inaccuracies in the luminance and chromatic values of a measured sample [10]. BRDF concept was also used for measuring and modeling of light reflected from paper [12], in computer graphics for photo-realistic rendering [13], in remote sensing field the BRDF concepts are applied for characterization of ground surfaces [14], and they are also used in the process of the designing luminaries [15].

Measuring reflectance spectra in thousands of different illumination–viewing combinations (called "geometries" here for simplicity) is not a very convenient method. Considerably lower number of measuring geometries is urgent for everyday work, especially when portable equipments are used to control the production or the products in situ. This requires shorter measurement time and application of suitable evaluation metrics to compare the results of similar samples. For this reason, much research has been done in the past to define the necessary measuring geometries for coatings with different classes of special effect pigments. Straightforward statistical analysis of BRDF data was done to reduce the massive number of measurement geometries required to characterize the appearance of coatings with special effect pigments having a complex directional appearance. The reduced number for the most complex sample was reported to be 1485 [16]. This is far too many for practical purposes in applications. The smallest number of measurement geometries sufficient to characterize gonioapparent samples is an important practical issue because it dictates the design of multi-angle spectrometers, which are useful to control the industrial products. Systematic research was performed to obtain this number for several classes of gonioapparent samples; reflection measurements under three different geometries were applied to characterize the appearance for coatings with metallic flakes [17,18]. At least six geometries were reported to characterize more complex gonioapparent materials with interference and/or diffraction effects [19], but approaches with five in-plane geometries were also reported [20]. The colorimetric capabilities of some coatings with special effect pigments were reported to be beyond MacAdam limits because of their unique optical properties [21]; however, in-plane measuring geometries are not sufficient for all complex optical phenomena. Therefore, off-plane measurement geometries were added. Several promising concepts were introduced to aid in the physical explanation of the results [22,23]. Flake-based parameters aid in the interpretation of multi-angle reflection data of effect coatings with very promising directions for further research [23]. Another approach proposes separation of BRDF into spectral and geometrical contributions; the concept was applied for better understanding of color variation in coatings with special effect pigments [24]. According to the best of our knowledge, there has been no research reported on the required measuring geometry for diffractive samples.

Commercial spectrometers with 6 (BYK-Mac®, BYK Gardner®), 19 (MA98®, X-Rite) and 98 (GK311/M®, Zeiss) measuring geometries exist. The latter of these is claimed to be sufficient for most complex effect coatings [23]. These spectrometers are dedicated to monitoring the optical properties of coatings with special effect pigments; therefore, they include the same 6 in-plane measuring geometries but the additional geometries are typically different. However, very little work was done on direct comparisons between bidirectional- and multi-angle spectrometers, according to the best of our knowledge.

Most research of BRDF concerns the visible spectral region which provides direct input for colorimetric calculations. In most cases, the data are in most cases represented as a matrix of spectral radiance coefficients or in goniocolorimetric space as the bidirectional color distribution function (BCDF) [9]. Another way to show the measurements is by plotting it as an sRGB image using polar coordinates [25]. As the BRDF data is challenging to represent, a polar coordinate sRGB image for a single illumination angle is very easy to understand and visually pleasing.

Another way to present BRDF data is to transform the measured reflectance data to the so-called goniospectrometric space, which provides a sort of optical fingerprint of a sample. Such a transformation was considered to be sufficiently simple for practical purposes and capable of providing information on the optical composition of a sample [26–28]. The inventors called their calculation method ″digital numerical analysis″ (DNA), which gives the xDNA curve. The second patent was assigned by X-Rite, Inc., who proposed the method with the MA98 multi-angle spectrometer software that has 11 in-plane and 8 off-plane geometries; however, independent scientific investigation of the method is lacking. This includes testing the validity of the most important claims brought forward by the authors:

- the 3D mathematical representation of an undersampled BRDF (called the xDNA curve) provides optical fingerprint of the sample;
- xDNA curves of similar samples have similar shape but are distinguishable in separable contributions; and
- the method greatly reduces the amount of data while preserv-

ing all the attributes of the gonioapparent appearance.

The above mentioned claims were tested by applying three types of optically complex samples:

a) diffraction gratings (DGs),

b) optically variable devices (OVDs), and

c) coatings with special effect pigments.

All the samples were provided from different sources, which means that they are real and meaningful samples. The properties that were not provided along the samples were analyzed applying conventional methods.

Diffraction gratings were selected because their optical properties can be calculated at arbitrary illumination–detection direction by applying diffraction theory [29]. This enabled the connection between the grating parameters and the goniometric reflectance, and its transformation into goniospectrometric space, the xDNA curve.

The complex gonioapparent effect with strong angular and spectral dependence can be obtained by optically variable devices (OVDs) used for optical security elements [30]. A typical OVD contains artwork of diffraction gratings with a period below a couple of micrometers, which is often combined with more complex structures. They are best viewed in conditions enabling first-order diffractions [30, 31]. Because they are, in general, diffractive by nature, the theoretical results obtained from the analysis of diffraction gratings are expected to be a good basis for studies of OVDs. Very little research can be found on the optical properties of OVDs. It was reported, that the angular dependent appearance of OVDs can be identified using a simple handheld optical microscope [32] whereas spectral imaging enables differentiation between genuine and counterfeit credit cards [33, 34]. No research has been found yet in which the BRDF of an OVD was analyzed.

The third type of studied optically complex samples were coatings with special effect pigments. Such coatings are one of the most commonly studied samples using goniospectrometric methods. We have selected them to compare our results with those from the literature and developed a more advanced approach for evaluation metrics. The most important types of such pigments are flakes made from metallic or transparent materials in single or layered forms, which provide reflection and/or scattering of light on interfaces [35–38]. The appearance of coatings with special effect pigments depends on the type of pigment, its size, size distribution, concentration, state of dispersion, orientation and orientation distribution [35,36]. Many of these parameters are believed to be controllable via coating technology. However, no systematic research has been reported on the orientation of flakes, and its consequences on appearance remain an interesting issue [39]. The lack of systematic research is due to the fact that it is not feasible to prepare coatings with variable parameters of the coating according to an arbitrary predetermined way. Instead, a suitable calculation model for optical properties of effect coatings is required. It was built using the concepts known from the literature [40,41], to enable calculating the BRDF of an effect coating with a known type of flakes and with arbitrary values of other coating parameters. The multi-angle reflectance spectra (BRDF) were transformed into the goniospectrometric space to obtain the xDNA curves. In this manner, the empirically based evaluation metrics, provided in some commercial software, were analyzed.

The aim of this study was:

- to aid physical explanations in the goniospectrometric research of the selected types of optically complex samples,
- to recommend a suitable calculation model for goniospectrometric reflectance of coatings with special effect pigments,
- to prove the three claims of the dynamic numerical analysis concerning the xDNA curves,
- to answer questions about the spectral and angular resolutions required for handheld multi-angle spectrometers,

- to recommend some simple procedures to compare optical properties of similar optically complex samples.

2 Samples

This chapter introduces the samples used in this study: diffraction gratings, optically variable devices (OVDs) and coatings with special effect pigments. It starts with an overall introduction of the diffraction gratings and OVDs, along with a description of the used samples. The second part of the chapter gives a theoretical overview of coatings with special effect pigments, which is followed by a description of different coatings used in this study.

2.1 DIFFRACTION GRATINGS AND OPTICALLY VARIABLE DEVICES (OVDS)

Diffraction gratings are periodic structures that diffract light into different directions. They have a single grating period and parallel straight-line grooves; the latter can be either exposed or buried, labeling diffraction gratings can then be labeled as overt or covert, respectively (Fig. 2.1). Overt diffraction gratings can be prepared by electroforming, etching or UV-diode laser ablation of a photoresist layer. Because their structure is open, it is relatively easy to analyze their structure, using AFM for example. In contrast, the covert diffraction gratings are made by alternating between a high refractive index material and polymer. Because their grating structure is buried, it can not be analyzed with AFM measurements; their period can often be measured with a confocal optical microscope, which does not provide any information about the amplitude of the grating or about the material used. Thus they are often used as semi-transparent overlays laminated on top of a document as security feature.

Figure 2.1: *Schematic representation of (a) overt and (b) covert diffraction grating. Also shown in the figures are grating period and amplitude.*

There were five diffraction gratings used in this thesis; three of them were overt and two were covert. Their descriptions along with grating periods and amplitudes are gathered in Table 2.1. The overt diffraction gratings were analyzed using AFM in order to obtain their parameters: grating period and amplitude. Contrary, only the period was obtained for covert diffraction gratings, using a confocal optical microscope.

Table 2.1: *Grating periods, type of the gratings and additional information of the diffraction gratings used in this study.*

sample	period (nm)	amplitude (nm)	type	additional info
DG1	350		covert	semitransparent overlay laminated on bare document page *
DG2	750	180	overt	electroformed
DG3	900		covert	semitransparent overlay **
DG4	1000	120	overt	etched
DG5	2500	40	overt	etched

* high-security Optoseal overlay with zero-order diffractive device, Hologram Industries (France), obtained in [30], Appendix, Figure A. 11.
** OVD Kinegram®, Switzerland.

Main criteria for the selection of diffraction gratings was their grating period, because it has the greatest influence on the reflectance spectra and consequently on goniospectrometric space curve. Thus, the selected gratings have their periods ranging from 350 nm to 2500 nm. They are also of two types; covert and overt diffraction gratings. The choice of two different types was done in order to study if and to what extent does the grating type influence the reflectance spectra and the goniospectrometric space curve.

Combining a collection of custom-based diffraction gratings creates a diffractive optically variable image device (DOVID) or an optically variable device (OVD). These are regarded as having the most complex gonioapparent effect, with strong angular and spectral dependence. Thus, they are commonly used as optical security elements for brand protection and document security with gratings forming a logo or some artwork. Their design is produced in order to have identifiable first-order diffractions best observable with point-source white light in non-specular conditions [30,31].

Four OVDs were used in the paper **IV**; this thesis presents other OVDs as well. Their descriptions are gathered in Table 2.2 and their photographs are included as Appendix A. The selection of the OVDs range from relatively simple ones, like OVD1, to highly complex ones, like OVD3. The type of the OVDs also differs; some are reflective while others are semitransparent overlays. The latter ones were included to evaluate the influence of the substrate on the reflectance spectra and the goniospectrometric space curve.

Table 2.2: *Description and size of the optically variable devices (OVDs) used in this study.*

sample	size (cm)	description
OVD1*	2×2	semitransparent overlay containing geometrically organized patches of gratings with a single period
OVD2*	3.5×3.5	
OVD3**	7×7	reflective dot-matrix hologram containing many diffractive security features
OVD4**	2.8×3.7	see-through foil with diffractive interferential optically variable image structure, laminated over the identification card
OVD5**	2.3×2.3	Exelgram made with electron beam lithography
OVD6**	2.5×2.5	Vectorgram made with electron beam lithography
OVD7**	5.6×5.6	Kinegram security device
OVD8**	2.1×2.1	Kinegram Secure Memory Card
OVD9**	2.6×2.6	Varimatrix hologram
OVD10**	2.4×2.9	HiMax OVD consisting of diffraction gratings, ″nanotext″, and ″nanologos″
OVD11**	2.4×2.9	BrandMax OVD consisitng of multiple optical effects
OVD12**	2.9×2.9	Chromagram - embossed diffractive surface coated with interference filter and pressed over paper
OVD13**	2.3×2.3	Chromagram - paper coated with optically variable adhesive
OVD14*	9×5.5	embossed transmissive holographic foil
OVD15*	8×5	
OVD16***	2.5×2.5	hot stamped reflective silver holographic foil

* Obtained from OVD Kinegram®, Switzerland.

** Obtained from Appendix A in [30].

*** Obtained from Optaglio®, Czech Republic.

2.2 COATINGS WITH SPECIAL EFFECT PIGMENTS

2.2.1 Theoretical description of coatings with special effect pigments

Coatings with special effect pigments are coating layers in which special effect pigments are distributed within a transparent binder, which is then coated over a substrate. A schematic representation of such a coating is shown in Fig. 2.2.

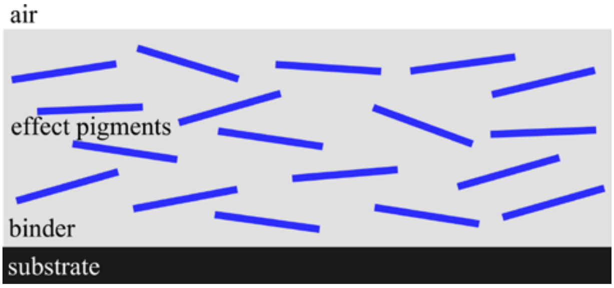

Figure 2.2: *Schematic representation of a coating with special effect pigments. Some coatings can have an additional layer on top for increased protection from the environments.*

The size of flake pigments can vary, from a couple of micrometers to some hundred micrometers. Smaller flakes produce more light scattered on the edges of the flakes than larger flakes do (Fig. 2.3). The shape of flakes can also vary due to different manufacturing processes (Fig. 2.4). The application of binder with effect pigments onto the substrate can have great influence on the flake's orientation and its distribution (Fig. 2.5). If the latter is small, the flakes are well oriented, and the coating has a glossy appearance. If the flake's orientation spread is large, the flakes are oriented randomly, and the coating appears matte. Another important parameter when applying the coating is volume concentration; with smaller values the effect of pigments becomes quite low, and the reflectance from the coating's substrate prevails.

Effect pigments can be classified into two groups; substrate-free pigments and multilayer/substrate-based pigments. Pigments from

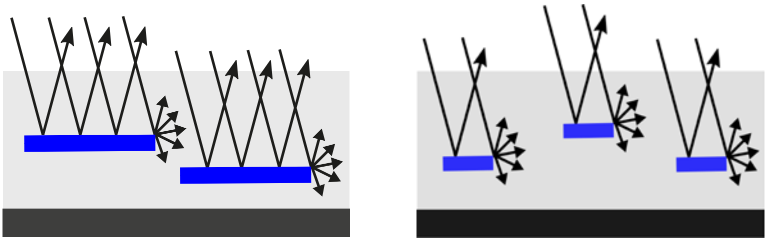

(a) **(b)**

Figure 2.3: *Schematic representation of reflection from (a) large and (b) small flakes. Smaller flakes produce more loss due to scattering on the edges.*

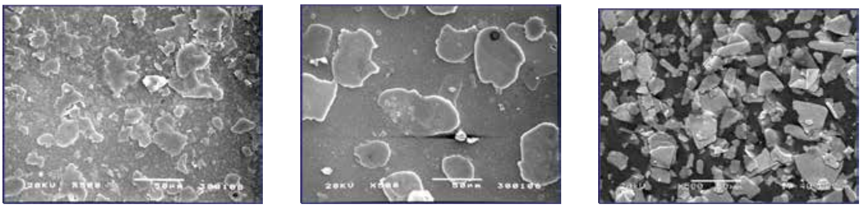

(a) **(b)** **(c)**

Figure 2.4: *SEM images of (a) "korn-like"-shaped aluminum, (b) "silver dollar"-shaped aluminum and (c) transparent pigments on the surface of selectively etched coating [42], which removed the top layer of the binder.*

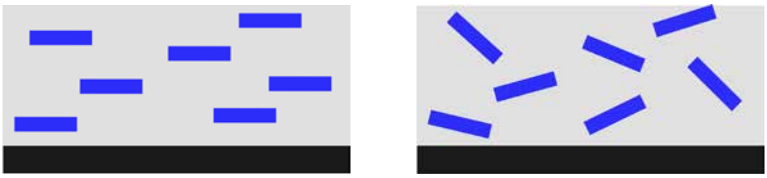

(a) **(b)**

Figure 2.5: *Schematic representation of coating with (a) small and (b) large flake's orientation spread.*

the former group consist of only one optically homogeneous material. By far the most important pigments of this group are metal effect pigments, which can be made from aluminum, copper, copper-zinc alloys, zinc or other metals. The metallic effect is caused by the reflection of light at the surface of the pigment's flake (Fig. 2.6a); they operate as little mirrors and reflect almost all incident light. [35–38].

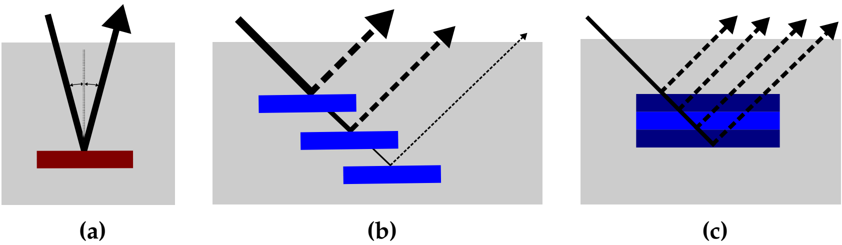

Figure 2.6: *Schematic representation of reflection from different types of pigments. (a) Specular reflection on metallic effect pigments, where almost all incident light is reflected. (b) Transparent pigments reflect some of the incoming light, and some they transmit, which produces the lustre effect. (c) Layered pigments show colors caused by interference on thin layers that make the flake pigment.*

Another example of substrate-free effect pigments is transparent pigments, with flakes that have a refractive index higher than that of a coating. The pearl lustre effect produced with these pigments is caused by partial reflection and partial transmission of light (Fig. 2.6b). Transparent pigments can be made either from natural pearl essence; a silky, lustrous suspension from fish scales, or from titanium dioxide (TiO_2). The former is very expensive, because it cannot be synthetically produced and is almost exclusively used only in expensive cosmetic applications. Titanium dioxide flakes are rather porous and brittle because they lack the mechanical support of a substrate. Thus, they are not used in applications where mechanical stress is induced. The thickness of these pigments vary in range of 40–50 nm for natural pearl essence, and 200–500 nm for titanium dioxide pigments [35,37,38].

Multilayer/substrate-based pigments have flakes with more than one material. Two or more layers of materials with different refractive indexes are used for multilayer pigments. In the case of substrate-based pigments, the flakes have a core; a substrate made from mica, silica, alumina, or metal. The most common core was natural mica, but substituting it with silica, SiO_2, offers three advantages: (1) the thickness of the SiO_2 can be more controlled, providing stronger interference color and smaller thicknesses (up to 50 nm); (2) since SiO_2 is synthetically produced, it does not have impurities which cause the slightly yellow tone of natural mica; (3) the interference effect is stronger because SiO_2 has lower refractive index than mica. Around the core is a layer (or layers) with a refractive index different than that of the core one. This causes interference on thin layers (Fig. 2.6c) and produces the color effect. Changing the thickness of flake's layers changes the observed color; therefore, it has a wide range of thicknesses available, from a few tens of nanometers to a few hundreds of nanometers. The most commonly used materials for the thin layer are Fe_2O_3 and TiO_2 [35,37,38].

2.2.2 Samples of coatings with special effect pigments

This study uses three sets of coatings with special effect pigments, labeled as M-, L- and T-set. Additionally it also uses a representative from the coating with metal lustre pigments from a Merck color card (Merck-Gruppe, Darmstadt, Germany), introduced in Paper **V**. The coating contains interference Iriodin 4504 pigments (Merck), which are mica-based flakes with a thin layer of iron (III) oxide (Fe_2O_3). The pigments were dispersed in an acrylic binder and coated on white paper. The specifications of the coating are given in Table 2.3. The thicknesses of the core material and Fe_2O_3 were not available for this pigment; however, the percentage of each material used in the pigment is specified by the producer. Thus, the thicknesses were adjusted, using the percentage information, by minimizing the color difference (CIE76) between the measured and calculated reflectance factor (see Figure 4 and Table 2 of Paper **V**).

Table 2.3: *Specifications of the coating with Iriodin 4504 metal lustre pigment: the materials of flakes, substrate and binder, the percentages of the flakes materials and the corresponding thicknesses used for calculations. The flakes are described as layer(s)/core/layer(s).*

	material(s)	thickness(es)
flakes	Fe_2O_3/mica/Fe_2O_3*	27.5%/45%/27.5% 74/121/74 nm
substrate	white paper	
binder	acrylic pitch	600 μm

* Optical constants of mica layer were substituted by those of SiO_2 for calculations.

All five coatings from M-set are applied on aluminum substrate and contain metal effect pigments: aluminum flakes. The flakes differ in size, shape and orientation. When we compare M1 and M2, we see that the first has pigments well-oriented parallel to the coating surface, while M2 has randomly oriented pigments (Figs. 2.7a and 2.7b). M2 also has an appreciable amount of pigments with damaged edges; in contrast, the M1 coating has almost circular shaped pigments with more or less smooth edges, so-called ″silver dollar″ pigments. Coatings M3–M5, made for the automotive industry, were obtained from three different manufacturers; they were prepared for the same color shade of metallic automotive coating. Aluminum pigments having different shape and size can be seen in SEM images in Figures 2.7c–2.7e. The three coatings are colorimetrically the same, meaning that their diffuse reflectance [42] has very similar values.

There are five different coatings with layered effect pigments in L-set; their specifications are gathered in Table 2.4. Since the thickness data are not available for these pigments, the percentage of each material used in the pigment, specified by the producer (Merck-Gruppe, Darmstadt, Germany), is given in the said table. The substrate for these coatings was white-coated aluminum with a thickness of 100 μm and the binder was 150 μm thick acrylic pitch.

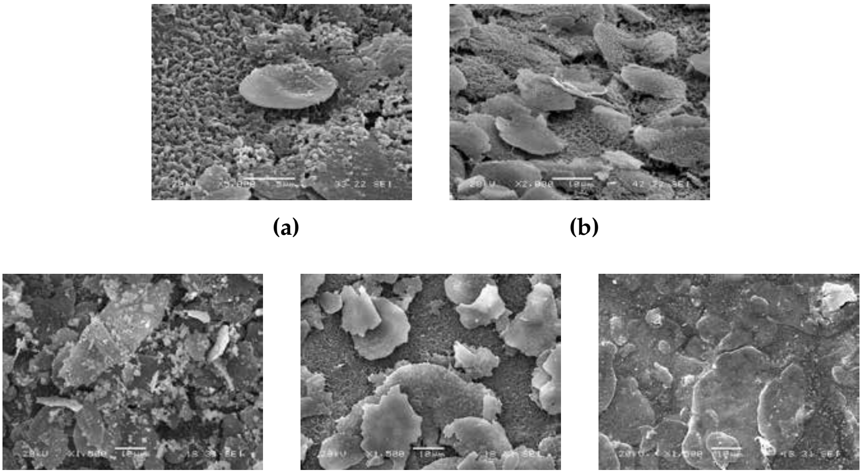

(a) **(b)**

(c) **(d)** **(e)**

Figure 2.7: *The SEM images for M-set coatings: (a) M1, (b) M2, (c) M3, (d) M4 and (e) M5 coating with metal effect pigments.*

Table 2.4: *Specifications of the coatings with layered effect pigments, L1–L5; type of pigments, the pigments materials and the percentage of those materials. The flakes are described as layer(s)/core/layer(s).*

	pigment	pigment materials	% of materials
L1	Xirallic T60-21	$TiO_2/SnO_2/Al_2O_3/SnO_2/TiO_2$	22/0.5/53/0.5/22
L2	Iriodin 7235	TiO_2/SnO_2/mica/SnO_2/TiO_2	34/0.5/32/0.5/34
L3	Iriodin 9103	TiO_2/SnO_2/mica/SnO_2/TiO_2	15/0.5/69/0.5/15
L4	Iriodin 9225	TiO_2/SnO_2/mica/SnO_2/TiO_2	25/0.5/49/0.5/25
L5	Iriodin 9502	Fe_2O_3/mica/Fe_2O_3	22/56/22

All the coatings were manufactured in two versions; with and without a cover layer; the latter was an acrylic pitch layer with a thickness of 50 μm.

T-set of coatings is a set with 16 different coatings with layered effect pigments, denoted here as T1–T16. Their specifications are gathered in Table 2.5. Not much was known about these samples; therefore, energy-dispersive X-ray spectroscopy (EDS) was performed on them in order to obtain the percentage of the materials used in the coatings.

Table 2.5: *Specifications of the coatings with layered effect pigments, obtained from Tikkurila (Finland); the pigments materials and the percentage of those materials, obtained by EDS measurements. The flakes are described as layer(s)/core/layer(s).*

	materials	percentage of each material (%)
T1	$TiO_2/ZnO/SiO_2/ZnO/TiO_2$	5/20.5/49/20.5/5
T2	$TiO_2/ZnO/SiO_2/ZnO/TiO_2$	23/5/44/5/23
T3	$TiO_2/ZnO/SiO_2/ZnO/TiO_2$	12.5/11/53/11/12.5
T4	$ZnO/SiO_2/ZnO$	21/58/21
T5	$ZnO/SiO_2/ZnO$	12/76/12
T6	$ZnO/SiO_2/ZnO$	26/48/26
T7	$ZnO/SiO_2/ZnO$	19/62/19
T8	$ZnO/SiO_2/ZnO$	21.5/57/21.5
T9	$ZnO/SiO_2/ZnO$	18.5/63/18.5
T10	$ZnO/SiO_2/ZnO$	22.5/55/22.5
T11	$ZnO/SiO_2/ZnO$	24/52/24
T12	$ZnO/SiO_2/ZnO$	9/82/9
T13	$ZnO/SiO_2/ZnO$	28/44/28
T14	$ZnO/SiO_2/ZnO$	13/74/13
T15	$Fe_2O_3/ZnO/SiO_2/ZnO/Fe_2O_3$	2.5/15/59/15/2.5
T16	$Fe_2O_3/ZnO/SiO_2/ZnO/Fe_2O_3$	2.5/14/61/14/2.5

3 Measurements

This chapter starts with a short overview of the bidirectional reflectance distribution function (BRDF). Then it proceeds with a description of the measuring devices; a commercial multi-angle spectrometer and a custom built bidirectional spectrometer. Lastly, the measuring geometries, used in this study, are introduced.

3.1 BIDIRECTIONAL REFLECTANCE DISTRIBUTION FUNCTION

The bidirectional reflectance distribution function (BRDF) is normally used to quantify the bidirectional reflectance measurements. It is defined as the ratio of the reflected radiance L_r and the incident irradiance E_i on the surface [1,2]

$$f_r(\theta_i, \phi_i, \theta_r, \phi_r) = \frac{L_r(\theta_i, \phi_i, \theta_r, \phi_r)}{E_i(\theta_i, \phi_i)} \tag{3.1}$$

where incident (θ_i, ϕ_i) and reflected angles (θ_r, ϕ_r) are as defined in Figure 3.1. Radiance L_r is the amount of radiant flux Φ_r, passing through a unit projected area, per unit solid angle $\mathrm{d}\Omega_r$:

$$L_r = \frac{\mathrm{d}\Phi_r}{cos\theta_r \mathrm{d}A \mathrm{d}\Omega_r} \tag{3.2}$$

with $\mathrm{d}A$ being the unit area. The latter along with the cosine term gives the projected unit area, which is perpendicular to the direction of propagation. Irradiance E_i is the amount of radiant flux passing through a surface per unit area:

$$E_i = \frac{\mathrm{d}\Phi_i}{\mathrm{d}A} \tag{3.3}$$

Combining Equations 3.2 and 3.3, and the assumptions that the illuminations spot is small, we obtain the following equation for BRDF:

$$f_r(\theta_i, \phi_i, \theta_r, \phi_r) = \frac{\mathrm{d}\Phi_r}{\mathrm{d}\Phi_i cos\theta_r \mathrm{d}\Omega_r} \tag{3.4}$$

We can see that the BRDF represents the flux reflected per unit projected solid angle [12,41].

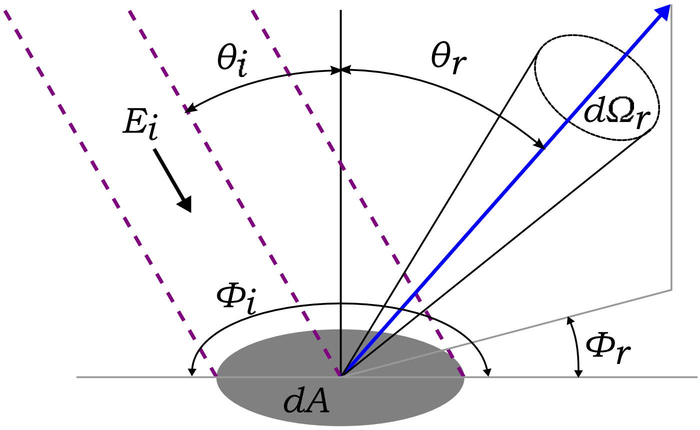

Figure 3.1: *Geometry of a goniometric measurement.*

Measurements of the BRDF can generally be divided into two different procedures: and absolute and a relative one. The former measuring procedure uses Equation 3.4; the incident irradiance and reflected radiance are measured separately by a single receiver. The absolute BRDF measurements have severe requirements for the instrument's mechanics: the aperture area and distance must be known, the detector should be able to be placed in the incident beam with the sample taken out of the way, and it should be linear over wide dynamic range [41].

Contrary, the relative BRDF measurements use a reference standard, which allows a simpler instrument design, since some of the requirements of the absolute measurement procedure are alleviated. It also increases the speed of the measurements, but the measurement accuracy is limited to that of the available standard. Since the relative BRDF procedure does not include measurements of the incident irradiance, reflectance factor R can be used [41]

$$R(\theta_i,\phi_i,\theta_r,\phi_r) = \frac{\mathrm{d}\Phi_r(\theta_r,\phi_r)}{\mathrm{d}\Phi_{ref}(\theta_r,\phi_r)}, \tag{3.5}$$

where $\mathrm{d}\Phi_{ref}(\theta_r,\phi_r)$ is radiant flux reflected by a perfectly reflecting

Lambertian diffuser in exactly the same measurement conditions. When BRDF is uniform, the collection angle has a very small solid angle and incident irradiation is unidirectional, the reflectance angle is related to BRDF as $R = \pi f_r$ [9,41].

3.2 MULTI-ANGLE SPECTROMETER

Multi-angle spectrometers are commonly used to control the optical properties of samples. In this work, the X-Rite MA98®, a portable multi-angle spectrometer, was used, which enables 19 measurement geometries. It measures 6 (-60°, -30°, -20°, 0°, 30°, 65°) and 5 (-60°, -30°, 0°, 30°, 65°) in-plane angles, using 45° and 15° illumination angles, respectively. The remaining 8 measuring geometries come from off-plane angles, which are the same for both illumination angles; $\theta_r = 50.1°$, $\phi_r = \pm 33.4°$, and $\theta_r = 45°$, $\phi_r = \pm 90°$. Measurement geometry for in- and off-plane angles is shown in Figure 3.2. The spectra are in the 400–700 nm spectral region with 10 nm wavelength steps. The measuring area of the device is 12 mm in diameter and the measurement time for all 19 geometries is within 2 s. The MA98 software comes with an in-built xDNA algorithm.

3.3 BIDIRECTIONAL SPECTROMETER

In order to measure samples with higher angular and spectral resolution, a bidirectional spectrometer was built. The design and evaluation of the device can be found in Paper **III**. Samples were illuminated by a halogen lamp at $\theta_r = 45°$and $\phi_r = 180°$ and measured at polar angles between 0° and 60° and all azimuthal angles in 2° angular steps. Even though the incident angle could be manually adjusted, it was set to 45° for all the samples measured during this study. This was done to somehow limit the number of changing parameters in measurements, while still using the incident angle normally applied in colorimetric measurements. Detection was done using a spectrometer Avantes AvaSpec-ULS2048XL with a wavelength range of 200–1160 nm and resolution of 0.6 nm.

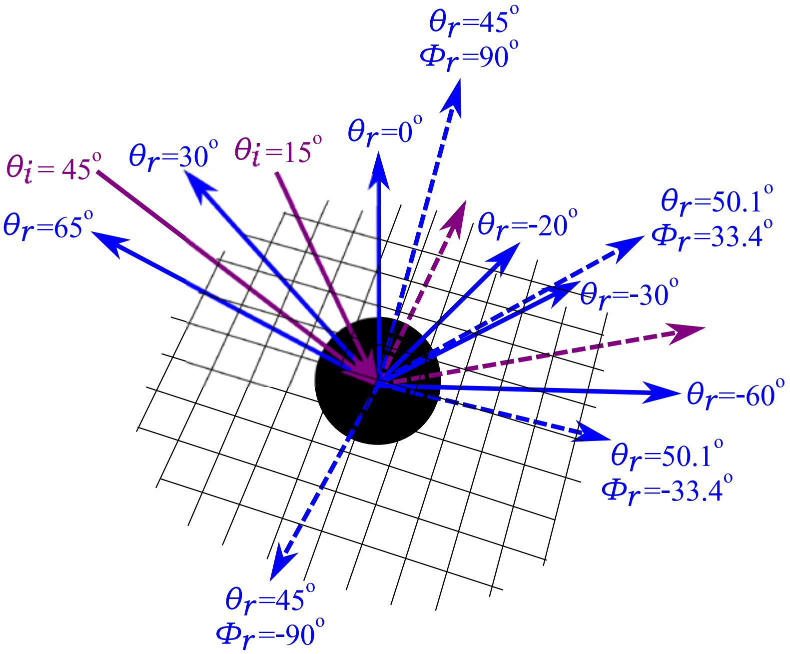

Figure 3.2: *Measurement geometry for X-Rite MA98 spectrometer, replicated from [43].*

The bidirectional spectrometer used automatically adjusting exposure time in order to provide maximum signal dynamics. Measurements were post-processed by subtracting environmental and detector noise and normalized according to angle and wavelength with 99% reflecting Spectralon, which served as a white reference.

3.4 MEASUREMENT GEOMETRIES

There are a number of measurement geometries used in this study, which are denoted as G6, G10, G17, G26 and Gn; all of them have the illumination angle $\theta_i = 45°$ (Table 3.1). Six in-plane measurement geometries with θ_r equal to -60°, -30°, -20°, 0°, 30° and 65° are denoted as a set of geometries G6. Also taking only in-plane angles, is set G17, in which θ_r goes from -80° to 80° with 10° steps. G10 measurement geometry takes in and off-plane measuring angles of an X-Rite MA98 multi-angle spectrometer with only a 45° illumination angle (see Figure 9a of Paper **IV** and chapter 3.2). Another geometry that includes off-plane angles is G26. Here, in-plane angles are the same as for G6 geometry, and off-plane angles are set at 20° and 40° polar angles, with the azimuthal direction going from ±30° to ±150° with 30° steps. When all angles that can be measured using the bidirectional spectrometer, are taken into account, we denote the measurement geometry as Gn. Here, polar angles from 0° to 60°, and all azimuthal angles, both with angle steps of 2°, are included; only angles around specular reflection are excluded.

Table 3.1: *Measurement geometries, all having the same illumination angle:* $\theta_i = 45°$. *Gn measurement geometry includes* $\theta_r = 0°$*: 2°: 60°, and* $\phi_r = -180°$*: 2°: 180°, excluding the angles around specular reflection.*

G6		G10		G17		G26	
θ_r	ϕ_r	θ_r	ϕ_r	θ_r	ϕ_r	θ_r	ϕ_r
-60°	0°	-60°	0°	-80°	0°	-60°	0°
-30°	0°	-30°	0°	-70°	0°	-30°	0°
-20°	0°	-20°	0°	-60°	0°	-20°	0°
0°	0°	0°	0°	-50°	0°	0°	0°
30°	0°	30°	0°	-40°	0°	30°	0°
60°	0°	60°	0°	-30°	0°	60°	0°
		50.1°	33.4°	-20°	0°	20°	30°
		50.1°	-33.4°	-10°	0°	20°	60°
		45°	90°	0°	0°	20°	90°
		45°	-90°	10°	0°	20°	120°
				20°	0°	20°	150°
				30°	0°	20°	-30°
				40°	0°	20°	-60°
				50°	0°	20°	-90°
				60°	0°	20°	-120°
				70°	0°	20°	-150°
				80°	0°	40°	30°
						40°	60°
						40°	90°
						40°	120°
						40°	150°
						40°	-30°
						40°	-60°
						40°	-90°
						40°	-120°
						40°	-150°

4 Numerical models

This chapter introduces the numerical models used in the study. Firstly, the numerical model for diffraction gratings is discussed. Secondly, the numerical model for coatings with special effect pigments is presented in details. And lastly, the calculations of goniospectrometric space curve are explained.

4.1 NUMERICAL MODEL FOR DIFFRACTION GRATINGS

The appearance of holographic structures is changed when their illumination angle and/or viewing angle are changed. This is a result of interference. However, regardless of whether a simple diffraction grating, or a complex OVD, which consists of diffraction grating patches, is under consideration, the theory behind the angle-dependent appearance is the same. The effect is best observed by illuminating the structure with a period smaller than the coherence length of visible light (a couple of micrometers) using white light, with the plane of incidence perpendicular to the grooves of the periodic structure. The diffracted light follows the grating equation [44]:

$$p = m\lambda/(\sin\theta_i + \sin\theta_m), \tag{4.1}$$

where p is the grating period, θ_i the incident angle, θ_m the diffraction angle, λ is the wavelength, and m is the order of the diffraction. The latter is positive when the diffraction angle is greater than the incident angle; the specular reflection yields $m = 0$; otherwise, the diffraction order is negative (Fig. 4.1). The incident angle is always taken to be positive, while the diffraction angle is positive, if it appears on the other side of the normal than the incident angle [44].

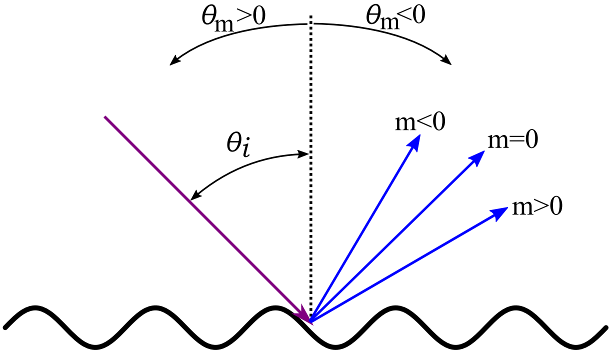

Figure 4.1: *Notation of illumination (θ_i) and diffraction (θ_m) angles and diffraction order (m).*

The intensity of the diffracted light consists of interference on the periodic structure and on the diffraction of light traveling from the light source to the sample and then to the detector/observer. It is expressed with the Fraunhofer diffraction integral [29]:

$$U(\xi) = \frac{e^{(ikz_0)}e^{(ik\xi^2/2z_0)}}{i\lambda z_0}\int_{-\infty}^{\infty} U(x)rect(\frac{x}{2w})e^{(-ikx\xi/z_0)}dx \qquad (4.2a)$$

$$U(x) = \frac{e^{(ikz_0)}e^{(ikx^2/2z_0)}}{i\lambda z_0}f(x)\int_{s_1}^{s_2} U_0 e^{(-ikxs/z_0)}ds \qquad (4.2b)$$

$$f(x) = e^{(ikna(1+\sin(2\pi x/p)))} \qquad (4.2c)$$

Parameters used in this numerical model are noted in Fig. 4.2, the model itself is described in greater detail in Paper **II**.

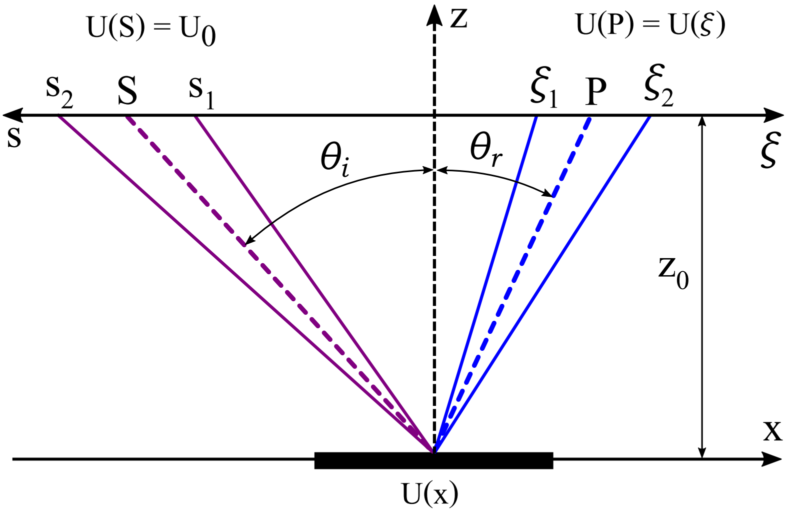

Figure 4.2: *Diffraction grating lies in plane x. It is illuminated at θ_i from plane s and measured at θ_r in plane ξ.*

4.2 NUMERICAL MODEL FOR COATINGS WITH SPECIAL EFFECT PIGMENTS

The numerical model presented in this section describes a scattering of light that impinges on a coating with special effect pigments [40, 41]. There are three parts of scattering that have to be incorporated in the model (see Fig. 2.2):

- scattering from the front surface of the sample; facet model
- scattering from effect pigments inside the sample; flake model
- scattering from the substrate; base model

The Stokes vector for scattering from the whole sample is thus described as:

$$S = (\mathbf{F}^{\mathbf{facet}} G(\theta_i, \theta_r) + \mathbf{F}^{\mathbf{flake}} G(\theta_i', \theta_r') + \mathbf{F}^{\mathbf{base}}) S_0 \tag{4.3}$$

where S_0 is the Stokes vector of the incident light, $\mathbf{F}^{\mathbf{model}}$ is the Mueller matrix BRDF for specific model, and G is the geometrical attenuation factor. The latter accounts for masking and shadowing of the light at large reflection angles and is defined by a set of formulas gathered in Equation 4.4 and Table 4.1 [45]:

$$G(\theta_i, \theta_r) = 1 - (1 - \sqrt{(1 - A(\theta_i, \theta_r)^2)}) / A(\theta_i, \theta_r) \tag{4.4a}$$

$$A(\theta_i, \theta_r) = \frac{\sin^2 \theta_r - \cos^2(\theta_r/2 - \theta_i/2)}{\cos^2(\theta_r/2 - \theta_i/2) - \cos(\theta_r - \theta_i) sin^2 \theta_r} \tag{4.4b}$$

where θ_i represents the incident angle, and θ_r the reflected angle. For the facet model, the geometrical attenuation factor, G, in Equation 4.3, is taken as it is; for the flake model, the incident and reflected angle, θ_i and θ_r, are replaced with θ_i' and θ_r'.

incident angle θ_i	reflection angle θ_r	equation
$0 \le \theta_i \le \frac{\pi}{4}$	$-\frac{\pi}{2} \le \theta_r \le \frac{\theta_i - \pi}{3}$	Eq. 4.4
	$\frac{\theta_i - \pi}{3} \le \theta_r \le \frac{\theta_i + \pi}{3}$	$G(\theta_i, \theta_r) = 1$
	$\frac{\theta_i + \pi}{3} \le \theta_r \le \frac{\pi}{2}$	Eq. 4.4
$\frac{\pi}{4} \le \theta_i \le \frac{\pi}{2}$	$-\frac{\pi}{2} \le \theta_r \le -\theta_i$	Eq. 4.4
	$-\theta_i \le \theta_r \le \frac{\theta_i - \pi}{3}$	Eq. 4.4 with θ_i and θ_r interchanged
	$\frac{\theta_i - \pi}{3} \le \theta_r \le \frac{\theta_i + \pi}{3}$	$G(\theta_i, \theta_r) = 1$
	$\frac{\theta_i + \pi}{3} \le \theta_r \le \frac{\pi}{2}$	Eq. 4.4

Table 4.1: *Equation for calculating geometrical attenuation factor,* $G(\theta_i, \theta_r)$*.*

4.2.1 Facet model

The facet model describes scattering from the front surface of the sample and is often referred to as the specular point theory in literature. Light is impinging the sample at an incident angle, θ_i, in respect to the mean surface normal. Reflected light is characterized by the reflected polar angle, θ_r, and the reflected azimuthal angle, ϕ_r. The local incident angle onto a facet, l, is defined as:

$$\cos l = \sqrt{\frac{1 - \sin\theta_i \sin\theta_r \cos\phi_r + \cos\theta_i \cos\theta_r}{2}} \tag{4.5}$$

The facet is assumed to be tilted at an angle θ_n, the cosine of which is determined as:

$$\cos\theta_n = \frac{\cos\theta_i + \cos\theta_r}{2\cos l} \tag{4.6}$$

Because the cosine is invariant to negative angles, we have to specify the sign of θ_n:

$$\theta_n = \begin{cases} +\theta_n & \text{if} \quad \theta_r < \theta_i \\ -\theta_n & \text{if} \quad \theta_r > \theta_i \end{cases} \tag{4.7}$$

The facet can also be tilted in the azimuthal direction; the facet azimuthal tilt angle also needs to be defined

$$\tan\phi_n = \frac{-\sin\phi_r \sin\theta_r}{\cos\phi_r \sin\theta_r - \sin\theta_i} \tag{4.8}$$

The slope of the facet, ζ, is also sometimes of interest; it is defined as a tangent of the facet tilt angle

$$\zeta = \tan\theta_n = \frac{\sqrt{\sin^2\theta_i + \sin^2\theta_r - 2\sin\theta_i \sin\theta_r \cos\phi_r}}{\cos\theta_i + \cos\theta_r} \tag{4.9}$$

The Mueller matrix BRDF, $\mathbf{F}^{\mathbf{facet}}$, for scattering from the front surface of the sample is computed as:

$$\mathbf{F}^{\mathbf{facet}} = \frac{P(\theta_n, \theta_0, \sigma)}{4\,\cos\theta_i\,\cos\theta_r\,\cos\theta_n}\mathbf{M}^{\mathbf{facet}} \tag{4.10}$$

where $P(\theta_n, \theta_0, \sigma)$ is the orientation distribution function. It can be described by many functions, and there is no clear preference for which is the best. In this thesis, the orientation distribution function used is logistic distribution with the mean facet tilt angle of θ_0 and standard deviation σ:

$$P(\theta_n, \theta_0, \sigma) = \frac{\exp\left(-\frac{\theta_n - \theta_0}{\sigma}\right)}{\sigma\left(1 + \exp\left(-\frac{\theta_n - \theta_0}{\sigma}\right)\right)^2} C \tag{4.11}$$

The C parameter in the equation is the fraction of the surface area covered by facets. Because the front surface covers the whole sample, the facet model is always computed using $C = 1$.

The Mueller matrix $\mathbf{M}^{\mathbf{facet}}$ is derived from the Jones matrix, $\mathbf{J}^{\mathbf{facet}}$, using the transformation

$$\mathbf{M} = \mathbf{U}\mathbf{J} \otimes \mathbf{J}^* / \mathbf{U} \tag{4.12}$$

with **U** being the transformation matrix given as

$$\mathbf{U} = \frac{1}{\sqrt{2}} \begin{bmatrix} 1 & 0 & 0 & 1 \\ 1 & 0 & 0 & -1 \\ 0 & 1 & 1 & 0 \\ 0 & i & -i & 0 \end{bmatrix} \tag{4.13}$$

The Jones matrix, $\mathbf{J}^{\mathbf{facet}}$, has the following elements:

$$q_{11}^{facet} = r_p(l)\sin\theta_i \sin\theta_r \sin^2\phi_r + a_2 a_3 r_s(l)/a_1 \tag{4.14a}$$

$$q_{12}^{facet} = -\sin\phi_r[a_2 r_p(l)\sin\theta_r - a_3 r_s(l)\sin\theta_i]/a_1 \tag{4.14b}$$

$$q_{21}^{facet} = -\sin\phi_r[a_3 r_p(l)\sin\theta_i - a_2 r_s(l)\sin\theta_r]/a_1 \tag{4.14c}$$

$$q_{22}^{facet} = r_s(l)\sin\theta_i \sin\theta_r \sin^2\phi_r + a_2 a_3 r_p(l)/a_1 \tag{4.14d}$$

where r_p and r_s are reflection coefficients for air/binder interface for p and s polarization and coefficients a_i are described as:

$$a_1 = \sin^2(2l) \tag{4.15a}$$

$$a_2 = \cos\theta_i \sin\theta_r + \sin\theta_i \cos\theta_r \cos\phi_r \tag{4.15b}$$

$$a_3 = \sin\theta_i \cos\theta_r + \cos\theta_i \sin\theta_r \cos\phi_r \tag{4.15c}$$

4.2.2 Flake model

Scattering from pigments inside a binder is regarded similarly to the facet model. It is necessary to take into account the refraction and the fact that pigments do not cover the entire sample area, but only a part of it. A simplified schematic of light scattering on flakes inside a coating is presented in Figure 4.3. Incident and reflected angles inside the coating are computed using Snell's law:

$$n_{binder}\sin\theta' = n_{air}\sin\theta \tag{4.16}$$

where n_{binder} and n_{air} are refractive indices for the binder and air, respectively.

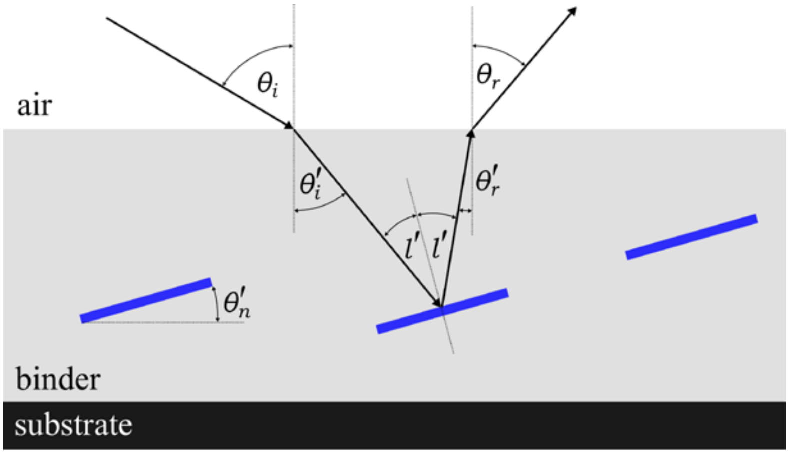

Figure 4.3: *Simplified schematic of light scattering on flakes inside a coating.*

Local incident angle onto a flake, l', is defined as:

$$\cos l' = \sqrt{\frac{1 - \sin\theta'_i \sin\theta'_r \cos\phi_r + \cos\theta'_i \cos\theta'_r}{2}} \tag{4.17}$$

and the flake tilt angle can be determined through following equation:

$$\cos\theta'_n = \frac{\cos\theta'_i + \cos\theta'_r}{2\cos l'} \tag{4.18}$$

As with the facet tilt angle, care must be taken with the sign of the angle because of cosines invariance. Equation 4.7 is re-used with the appropriate flake tilt angle, instead of the facet tilt angle. The azimuthal direction of flake tilt angle, $\tan\phi'_n$, and slope of the flake, ζ', are defined similarly as for facet case:

$$\tan\phi'_n = \frac{-\sin\phi'_r \sin\theta'_r}{\cos\phi'_r \sin\theta'_r - \sin\theta'_i} \tag{4.19}$$

$$\zeta' = \tan\theta'_n = \frac{\sqrt{\sin^2\theta'_i + \sin^2\theta'_r - 2\sin\theta'_i \sin\theta'_r \cos\phi_r}}{\cos\theta'_i + \cos\theta'_r} \tag{4.20}$$

Mueller matrix BRDF, $\mathbf{F}^{\mathbf{flake}}$, for scattering from flakes inside a coating is computed as:

$$\mathbf{F}^{\mathbf{flake}} = \frac{P(\theta'_n, \theta'_0, \sigma')\, n^2_{binder}}{4\, \cos\theta_i\, \cos\theta_r\, \cos\theta'_n}\, \mathbf{M}^{\mathbf{flake}} \tag{4.21}$$

The orientation distribution function, $P(\theta'_n, \theta'_0, \sigma')$, is computed using Equation 4.11 with appropriate flake tilt angle, θ'_n, mean flake tilt angle, θ'_0, and distribution variance, σ'. C parameter from the equation plays a more important role in the flake model. If it is equal to 1, the whole sample is covered with flakes. If there are no flakes inside a coating, the parameter will be zero. The flake size and volume concentration are directly related to the surface coverage parametrized by C.

The Mueller matrix $\mathbf{M}^{\mathbf{flake}}$ is derived from the Jones matrix $\mathbf{J}^{\mathbf{flake}}$ with the following elements:

$$q^{flake}_{11} = t_s(\theta_i)t_s(\theta_r)[r'_p(l')\sin\theta'_i \sin\theta'_r \sin^2\phi_r + a'_2 a'_3 r'_s(l')]/a'_1 \tag{4.22a}$$

$$q^{flake}_{12} = -t_s(\theta_i)t_p(\theta_r)\sin\phi_r[a'_2 r'_p(l')\sin\theta'_r - a'_3 r'_s(l')\sin\theta'_i]/a'_1 \tag{4.22b}$$

$$q^{flake}_{21} = -t_p(\theta_i)t_s(\theta_r)\sin\phi_r[a'_3 r'_p(l')\sin\theta'_i - a'_2 r'_s(l')\sin\theta'_r]/a'_1 \tag{4.22c}$$

$$q^{flake}_{22} = t_p(\theta_i)t_p(\theta_r)[r'_s(l')\sin\theta'_i \sin\theta'_r \sin^2\phi_r + a'_2 a'_3 r'_p(l')]/a'_1 \tag{4.22d}$$

where r'_p and r'_s are reflection coefficients for the binder/flake interface for p and s polarization, and t_p and t_s are transmission coefficients for the air/binder interface for p and s polarization. Coefficients a'_i are described as:

$$a'_1 = \sin^2(2l') \tag{4.23a}$$

$$a'_2 = \cos\theta'_i \sin\theta'_r + \sin\theta'_i \cos\theta'_r \cos\phi_r \tag{4.23b}$$

$$a'_3 = \sin\theta'_i \cos\theta'_r + \cos\theta'_i \sin\theta'_r \cos\phi_r \tag{4.23c}$$

4.2.3 Base model

The base model incorporates scattering from the substrate. According to this model, light can take four different paths on its way through the coating towards the substrate and back. The paths, along with the corresponding angle notations are schematically represented in Figures 4.4 and 4.5, and expressed as:

1. transmission through pigments, diffuse reflection from the substrate, transmission returning through pigments
2. transmission through the binder (no crossing of pigments), diffuse reflection from the substrate, transmission returning through pigments
3. transmission through pigments, diffuse reflection from the substrate, transmission returning through binder (no crossing of pigments)
4. transmission through the binder (no crossing of pigments), diffuse reflection from the substrate, transmission returning through the binder (no crossing of pigments)

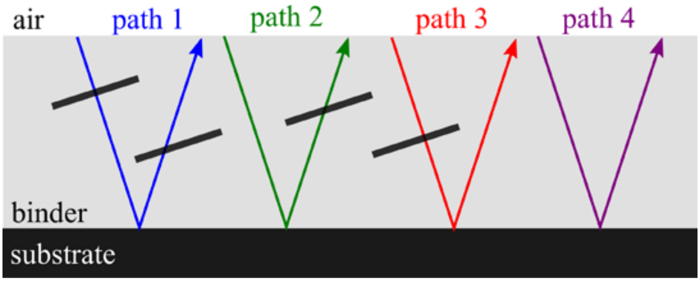

Figure 4.4: *Schematic representation of the four different paths the light can follow when undergoing scattering from the substrate. For simplicity, only four flake pigments are drawn.*

Besides the described four paths, incorporated in the base model, the light can also take other paths on its way through the coating towards the substrate and back. For example, the light can traverse

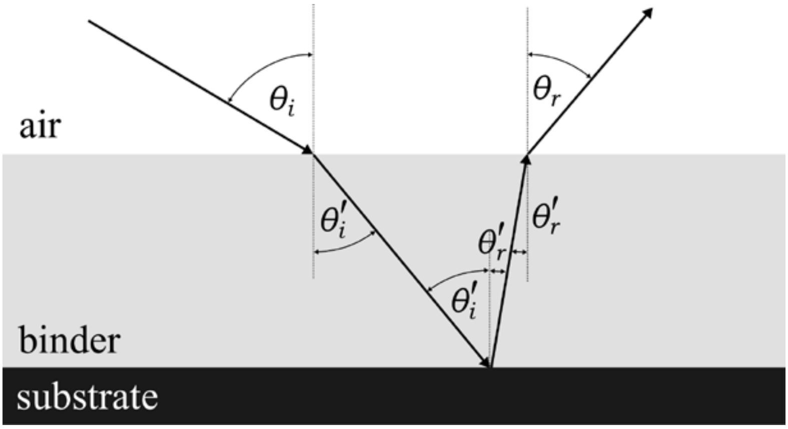

Figure 4.5: *Schematic representation of angles used in the base model. Only the fourth path is shown. For other three paths, the angles are the same; we only add pigment on the corresponding side(s).*

through the pigment, reflects from the substrate, then reflects from the pigment, reflects again from the substrate, and traverses either through a pigment or the binder before exiting the coating. This multiple reflection component represents only a very small portion of the overall reflection, therefore it is not included in the numerical model.

The first path will always occur to some extent, being the only possible path in the case of complete coverage ($C = 1$), whereas the other three can occur only if $C < 1$. Mueller matrices BRDF for the four different paths are computed as:

$$\mathbf{F}^{\mathbf{path1}} = \frac{P(\theta'_n, \theta'_0, \sigma')\, n^2_{binder}}{4\cos\theta_i\,\cos\theta_r\,\cos\theta'_n}\,\mathbf{M}^{\mathbf{path1}} \tag{4.24a}$$

$$\mathbf{F}^{\mathbf{path2}} = \frac{P(\theta'_n, \theta'_0, \sigma')\, n^2_{binder}}{4\cos\theta_i\,\cos\theta_r\,\cos\theta'_n}\,(1-C)\,\mathbf{M}^{\mathbf{path2}} \tag{4.24b}$$

$$\mathbf{F}^{\mathbf{path3}} = \frac{P(\theta'_n, \theta'_0, \sigma')\, n^2_{binder}}{4\cos\theta_i\,\cos\theta_r\,\cos\theta'_n}\,(1-C)\,\mathbf{M}^{\mathbf{path3}} \tag{4.24c}$$

$$\mathbf{F}^{\mathbf{path4}} = (1-C)^2\,\mathbf{M}^{\mathbf{path4}} \tag{4.24d}$$

and the Mueller matrices are computed from the Jones matrices:

$$\mathbf{J^{path1}} = \begin{bmatrix} q_{11}^{flake} t_s'(l')^2 & q_{12}^{flake} t_s'(l') t_p'(l') \\ q_{21}^{flake} t_s'(l') t_p'(l') & q_{22}^{flake} t_p'(l')^2 \end{bmatrix} \tag{4.25a}$$

$$\mathbf{J^{path2}} = \begin{bmatrix} q_{11}^{flake} t_s'(l') & q_{12}^{flake} t_p'(l') \\ q_{21}^{flake} t_s'(l') & q_{22}^{flake} t_p'(l') \end{bmatrix} \tag{4.25b}$$

$$\mathbf{J^{path3}} = \begin{bmatrix} q_{11}^{flake} t_s'(l') & q_{12}^{flake} t_s'(l') \\ q_{21}^{flake} t_p'(l') & q_{22}^{flake} t_p'(l') \end{bmatrix} \tag{4.25c}$$

$$\mathbf{J^{path4}} = \begin{bmatrix} t_s(\theta_i) t_s(\theta_r) r_s''(l') & 0 \\ 0 & t_p(\theta_i) t_p(\theta_r) r_p''(l') \end{bmatrix} \tag{4.25d}$$

where r_s'' and r_p'' are reflection coefficients for the interface binder-substrate.

4.3 GONIOSPECTROMETRIC SPACE CURVE

The goniospectrometric space curve, also known as the xDNA curve, is a 3D graph that is capable of providing information about the optical composition of a sample and is considered sufficiently simple for practical purposes [26,27]. The special mathematical transformation of BRDF data was termed "digital numerical analysis" (DNA), and it results in an xDNA graph. It is a simple representation of the BRDF data with the number of measurement geometries adjusted as desired. The goniospectrometric space curve is obtained via the summation of BRDF data over all measurement geometries:

$$\mathbf{xDNA} = \mathbf{R}\boldsymbol{\mu} \tag{4.26}$$

where $\mathbf{R}$ is an $k \times n$ matrix with spectral data; k is the number of wavelengths λ, and n counts viewing directions. **xDNA** is an $k \times 3$ matrix and $\boldsymbol{\mu}$ is an $n \times 3$ matrix of viewing directions expressed as:

$$\mu^x = \sin\varphi_{as} \sin\varphi_{az} \tag{4.27a}$$

$$\mu^y = \sin\varphi_{as} \cos\varphi_{az} \tag{4.27b}$$

$$\mu^z = \cos\varphi_{az} \tag{4.27c}$$

where φ_{as} and φ_{az} are aspecular and off-plane angle, respectively. Axes are oriented as shown in Figure 4.6b; the z-axis is oriented in the specular direction, the y-axis lies in the plane of incidence and the x-axis is perpendicular to them.

The resulting xDNA graph is, in general, a 3D curve. If there are no off-plane reflections, the xDNA curve is two-dimensional, extending only in the (y, z) plane. Schematic representation of the calculation for one wavelength, giving one point in the xDNA curve, is shown in Figure 4.6 and a simplified calculation for a two-dimensional xDNA curve from reflectance spectra is shown in Figure 4.7.

DNA transformation uses angles expressed in xDNA coordinates. Thus, we need the connection between those angles $(\varphi_{as}, \varphi_{az})$ and angles in spherical coordinates $(\theta_i, \theta_r, \phi_r)$. The connection is visually represented in Figure 4.8. Aspecular angle φ_{as} for in-plane

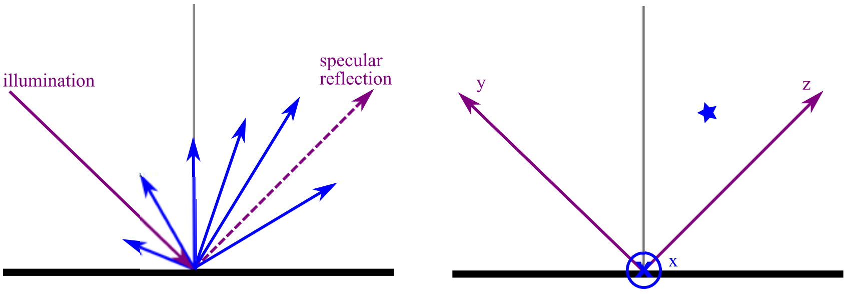

(a) **(b)**

Figure 4.6: *(a) Reflection for one wavelength at 6 angles marked as blue lines with length representing the intensity in the given direction. Illumination and specular direction are marked in purple. (b) After xDNA transformation a single point (marked by blue star) is obtained in goniospectrometric space. Also marked on the graph are coordinates; axes x, y and z.*

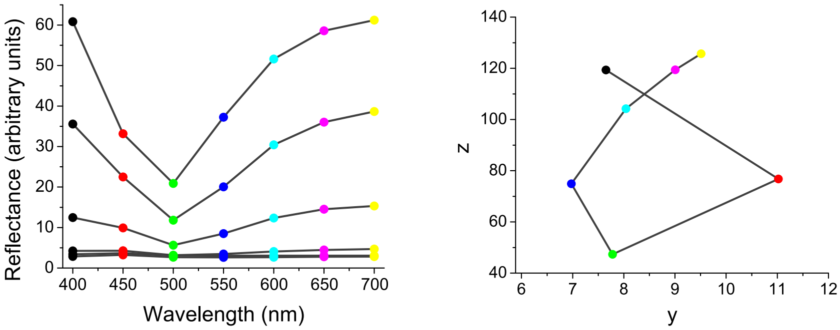

(a) **(b)**

Figure 4.7: *(a) Reflectance spectra for 6 viewing angles, with marked wavelength points (b) and its corresponding xDNA curve. Color points on xDNA curve match in color the wavelength points in (a).*

angles can be simply expressed as [18]:

$$\varphi_{as} = \theta_i + \theta_r \tag{4.28}$$

where θ_i is the incident angle and θ_r thereflected polar angle. For off-plane angles, the transformation is expressed as a set of equations:

$$a = \sin\theta_i + \tan\varphi_{as}\cos\varphi_{az}\cos\theta_i \tag{4.29a}$$

$$b = \tan\varphi_{as}\sin\varphi_{az} \tag{4.29b}$$

$$c = \cos\theta_i + \tan\varphi_{as}\cos\varphi_{az}\sin\theta_i \tag{4.29c}$$

$$\theta_r = \arctan(b/a) \tag{4.29d}$$

$$\phi_r = \arccos(c/\sqrt{a^2+b^2+c^2}) \tag{4.29e}$$

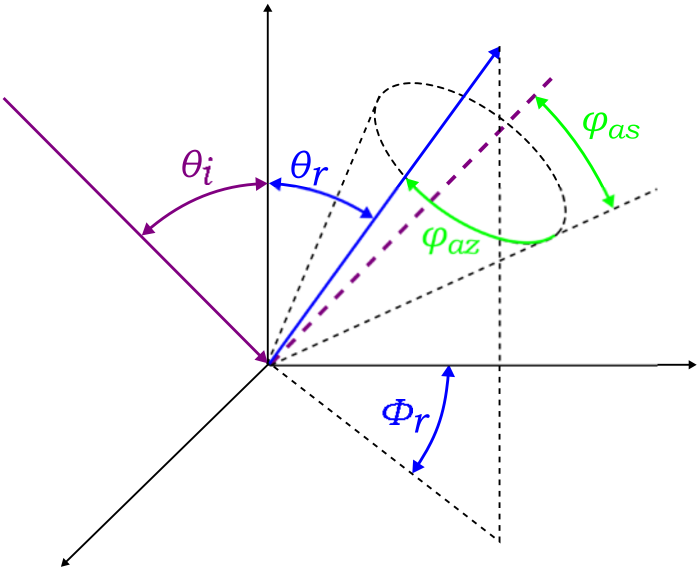

Figure 4.8: *Description of detection direction for illumination at θ_i. It is presented in a polar coordinate system with polar (θ_r) and azimuthal angles (ϕ_r) and with American Society for Testing and Materials (ASTM) notation by aspecular (φ_{as}) and azimuthal angles (φ_{az}).*

5 Results

In this chapter, we present the summarized results of the goniospectrometric space curves for different samples. We start with some exemplary samples and continue with the goniospectrometric space curves of diffraction gratings and optically variable devices (OVDs). Finally, the goniospectrometric space curves of coatings with special effect pigments are described.

5.1 GONIOSPECTROMETRIC SPACE CURVE OF EXEMPLARY SAMPLES

The ability of goniospectrometric space curves to present the optical fingerprint of measured samples is the main topic of Paper **I**. It presents xDNA curves of differently smooth bulk samples and of samples with differently thick surface layers prepared from the same material. All examples in this chapter were measured using an X-Rite MA98 multi-angle spectrometer using all the available measuring geometries; two illumination angles ($\theta_i = 45°$ and $\theta_i = 15°$) and 19 measuring angles (see chapter 3.2), denoted here as geometry G19.

The influence of surface roughness/smoothness was analyzed using differently rough silicon wafers, from which light reflects only from the surface. Polished silicon wafer acts as a metallic mirror that reflects practically all light in the specular direction and as a consequence its xDNA curve is essentially a point located almost at the origin of the goniospectrometric space (Fig. 5.1). Unpolished silicon wafers have the highest reflectance at specular direction but opposite to the polished silicon wafer; other directions, especially near the specular direction, also reflect. This results into a line in the goniospectrometric space (Fig. 5.1). The orientation of the line shows diminishing reflectance with a wavelength in all measurement geometries. The greater roughness of silicon results in larger absolute y values, since there is more light reflected outside the specular reflection. x values are related to off-plane measuring directions; flakes with smoother edges reflect more in those directions, which results in bigger x values.

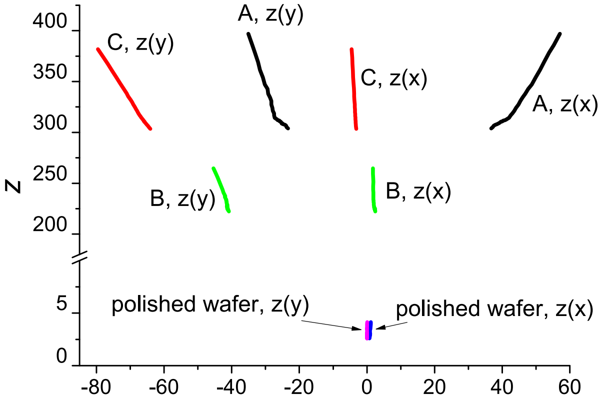

Figure 5.1: *xDNA curves of polished and unpolished silicon wafers for G19. The latter are labeled as A, B and C for having the lowest to greatest amount of roughness, respectively.*

Similarly to silicon wafers, white paper also has little spectral dependence in the visible part of the spectrum. Double-side coated white paper, which was used here, has one side calendered to a smooth and glossy surface, and the other, uncalendered, looks matte. xDNA curves for both sides of the paper look similar (see Figure 7 of Paper **I**); there is almost no reflection in off-plane directions, resulting in negligible x values. In contrast, the yz plane gives line-shaped xDNA curves, which are parallel for the calendered and uncalendered sides of the white paper. The length of the xDNA curves depends on the roughness; a lower roughness results in a longer xDNA curve.

From the bulk samples, we move to samples with differently thick layers; transparent interference layers. Silicon nitride was deposited on the polished silicon wafer in different thicknesses; 220 nm, 390, and 635 nm. The xDNA curve for these samples is a loop in the yz plane and practically a line in the xz plane. The latter is a result of very small reflectance in the off-plane angles. The number of interference peaks in reflectance spectra (see Figure 8 of Paper **I**) corresponds to the number of loops in the xDNA curve.

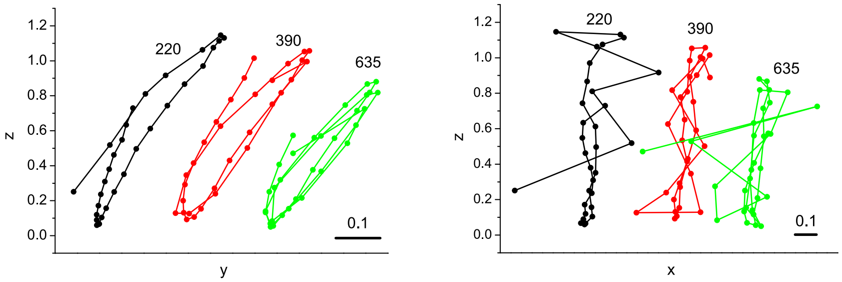

(a) **(b)**

Figure 5.2: *(a) xDNA curves in yz and (b) xz projections for silicon nitride films using G19. The thickness is labeled next to the curves in nm. xDNA curves in both graphs are split horizontally (on the y/x axis) for clarity.*

Another example of an interference layer was prepared as a clear varnish with a thickness between 0.12 and 0.29 μm, applied on a black and white matte cardboards. The interference colors are almost invisible on the white cardboard; on black paper, the thinnest layers give blue and the thickest give yellow-gold color. An interference layer on the black substrate produces a loop in the xDNA curve (Fig. 5.3), as a result of one interference peak in reflectance spectra (see Figure 9 of Paper **I**). This is consistent with the results for silicon nitride on a polished silicon wafer. The white cardboard reflects more in comparison to the black one, producing a smaller interference peak. As a result, the xDNA curve is a line, characteristic of white paper, with a loop, characteristic for an interference layer.

For comparison, pigmented coatings with similar thicknesses as the interference layers were measured. The magenta offset thermochromic ink was applied on the glossy side of white paper in thicknesses between 120 and 440 nm with an 80 nm step. The selective absorption of the magenta ink increases with thickness, pro-

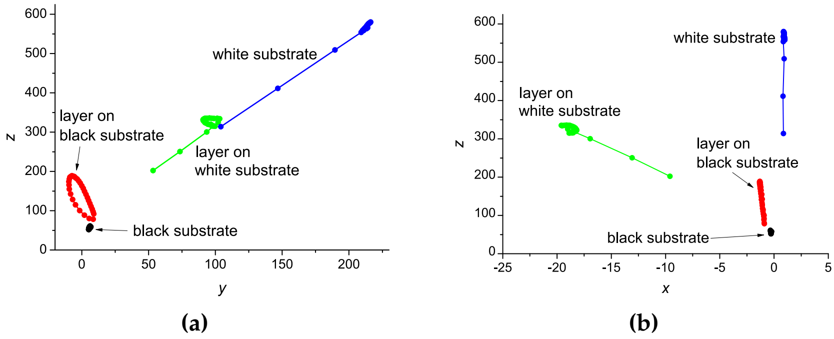

Figure 5.3: *(a) xDNA curves in yz and (b) xz planes as measured for thin varnish layers on black and white cardboards using G19. The xDNA curves of the black and white cardboard are also shown.*

ducing a deeper color. Since there is no interference, the resulting xDNA curves are parallel lines, similar to that of the white paper. Differing from the latter, the xDNA curve of magenta ink has an additional flat loop due to spectral absorption, that increases with a layer's thickness.

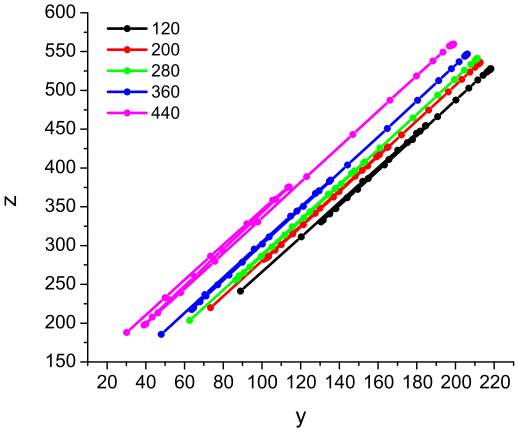

Figure 5.4: *xDNA curves for thin layers of the magenta ink printed on white glossy paper using G19. Layer thicknesses are labeled in the legend in nm.*

Analysis of exemplary samples was crucial in order to confirm that the goniospectrometric space curve could serve as an appearance fingerprint. The characteristic shapes of xDNA curves in all optically similar samples appear consistently. Differently rough samples of the same material could be distinguished using xDNA curves. The method could also be used to detect the existence of a transparent layer with thickness beyond the coherence length of white light. Paper **I** opened the door for a systematic research of goniospectrometric space curve of diffraction gratings, OVDs, and coatings with special effect pigments.

5.2 GONIOSPECTROMETRIC SPACE CURVE OF DIFFRACTIVE SAMPLES

Papers **II** and **IV** present the goniospectrometric space curve of diffractive samples; diffraction gratings and optically variable devices (OVDs). There are a number of parameters that can be varied, such as spectral and angular resolution, amplitude and grating period. These two papers explore how these parameters affect the xDNA curves.

5.2.1 Effect of spectral resolution

First, the effect of spectral resolution on goniospectrometric space curves was evaluated; xDNA curves for samples having wavelength steps of 1 and 10 nm were compared. In both cases, the xDNA curves had practically the same shape with the xDNA curve for 1 nm spectral resolution having more points. Paper **II** confirmed this result theoretically while Paper **IV** used measurements of a simple diffraction grating DG2, with a grating period of 750 nm, and a more complex OVD sample OVD1 (see Fig. A.1), having 4 different grating periods. Both samples are described in greater detail in Paper **IV**. Figure 5.5 shows xDNA curves obtained with 10 and 1 nm wavelength steps for DG2 and OVD1. The results reveal that the goniospectrometric space conversion can be done using lower spectral resolution, since most optical properties of diffractive samples are described with it. Therefore, in the rest of this thesis, the 10 nm wavelength step will be used.

5.2.2 Dependence on grating amplitude

Dependence on the amplitude of the diffraction gratings was evaluated using theoretical reflectance spectra in Paper **II**. Phase shift $f(x)$, which occurs at the sample surface, is defined by the grating amplitude (Eq. 4.2c). Consequently, a larger grating amplitude results in higher reflectance. Similarly, it results in a larger xDNA curve. Figure 5.6 shows xDNA curves obtained for diffraction grat-

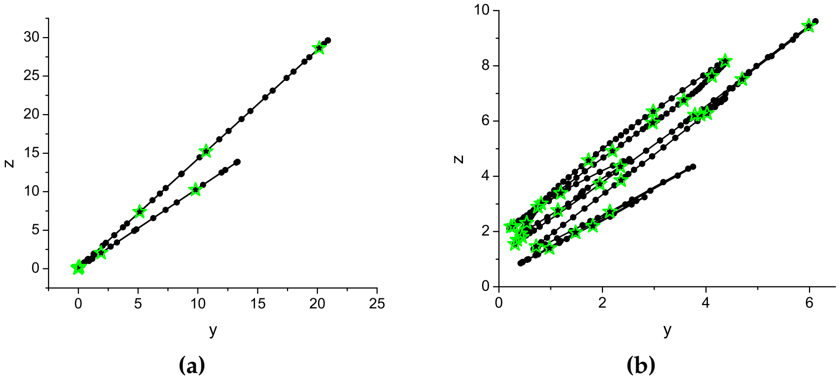

(a) **(b)**

Figure 5.5: *Comparing xDNA curves for spectral resolution of 10 nm (green symbols) and 1 nm (black symbols) for (a) a diffraction grating DG2 with a grating period of 750 nm for G6, and (b) a more complex sample OVD1, having 4 grating periods, ranging from 666 nm to 3080 nm for G10.*

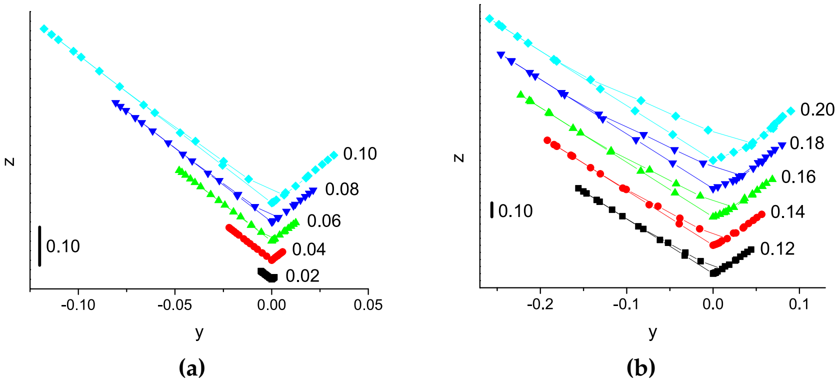

(a) **(b)**

Figure 5.6: *xDNA curves for diffraction gratings with a grating period 3.5 μm and an amplitude range of (a) 0.02 to 0.10 μm, and (b) 0.12 to 0.20 μm. The amplitude values are specified in the graphs, in μm. All xDNA curves emerge from (0,0) but are split vertically (on the z-axis) for clarity. The reader should pay attention to the different y scales of the two graphs. The geometry applied is G6.*

ings having a grating period of 3.5 μm and amplitude ranging from 0.02 to 0.2 μm. When amplitude decreases, the xDNA curve shrinks to just a point at $y = z = 0$. This describes a flat surface, such as a polished silicon wafer (see Fig. 5.1). At amplitude values smaller or equal to 0.1 μm, two lines are obtained in the xDNA graph, corresponding to two diffractions occurring at $\theta_r = -60°$ and $\theta_r = -30°$ (see Figure 3 of Paper **II**). When the amplitude is larger than 0.1 μm, the xDNA curve becomes more distinct due to two additional diffractions at $\theta_r = -20°$ (see Figure 4 of Paper **II**).

5.2.3 Dependence on grating period

The spectral position of the diffraction is determined by the grating period. Bigger period shifts the diffraction peaks towards larger wavelengths. Fig. 5.7 shows xDNA curves for diffraction gratings with an amplitude of 0.03 μm and grating periods ranging from 0.4 to 4 μm. Amplitude was chosen so that only first order diffractions are relevant. This means that the reflectance spectra of diffraction gratings are transformed into a line emerging from $(0, 0)$. The slope of the line is related to the diffraction angle, and its length to the intensity of the diffraction.

The relation between slope of the xDNA curve and the aspecular angle at which the diffraction occurs has been analyzed in Paper **II** and Paper **IV**. xDNA curves of diffraction gratings with amplitude of 0.03 μm and 18 different periods ranging from 0.35 to 5 μm were calculated for G6 measurement geometry and for 32 reflection angles from $-80°$ to 80°, with 5° step and excluding specular reflection at 45°. Figure 3 of Paper **IV** shows the relation between the slope of the obtained diffraction lines and aspecular angle at which the diffraction occurs. A similar graph is also shown as Figure 10 of Paper **II**, where the grating period range was smaller (between 1 and 3.5 μm). There is an almost linear correlation between slope and aspecular angles, with a local minimum at larger aspecular angles.

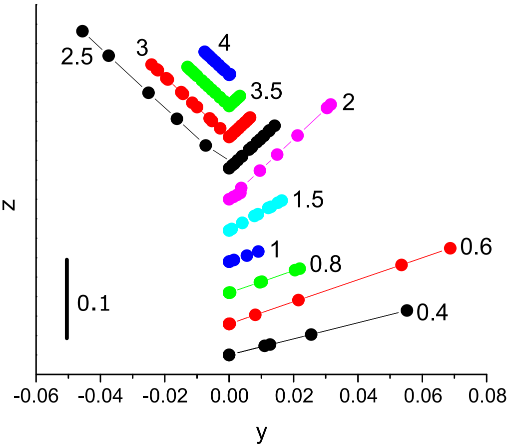

Figure 5.7: *xDNA curves in dependence on grating period marked next to the curves in µm and with amplitude of 0.03 µm. All xDNA curves emerge from* $(0, 0)$ *but are split vertically (on the z axis) for clarity. The geometry applied is G6.*

The theoretical correlation between slope and aspecular angles was confirmed with measurements presented in Paper **IV**. Five diffraction gratings with periods ranging from 350 to 2500 nm were measured, and their reflectance spectra were transformed to goniospectrometric space. The correlation between the slope of xDNA lines and the aspecular angle is in accordance with theoretical calculations. These results confirmed that the xDNA graph is indeed a unique representation of the diffraction grating for the case of G6 measurement geometry. The grating period of the sample can be obtained from the slope of the xDNA curve, with the use of the correlation between slope and aspecular angle.

5.2.4 Influence of angular resolution

The influence of angular resolution was shown for theoretical calculations comparing G6 and G17 measurement geometries in Paper **II**, and for measurements in Paper **IV** comparing G6 and G10 for diffraction gratings and OVDs, respectively, with measurement geometries G26 and Gn. Comparisons are shown in Figures 5.8–5.10.

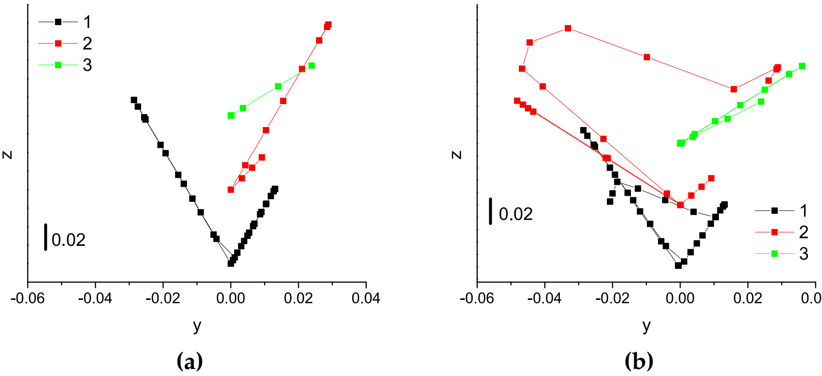

(a) **(b)**

Figure 5.8: *Dependence of xDNA curves of gratings with amplitude 0.03 μm on period (indicated in the legend in μm) calculated for (a) G6 and (b) G17 measurement sets. All xDNA curves emerge from (0,0) but are split vertically (on the z-axis) for clarity.*

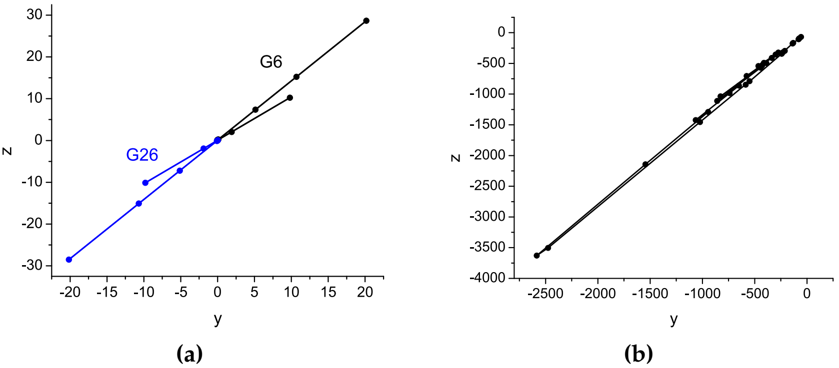

(a) **(b)**

Figure 5.9: *(a) The xDNA curve of DG2 in the G6 and G26 measurement geometry and (b) in Gn measurement geometry.*

In all cases, it was shown that more diffractions obtained with more geometries results in a higher number of interconnections between diffraction lines (lines representing spectrally isolated diffractions) in the xDNA graphs. With enough measuring geometries, the xDNA curve for either diffraction grating or OVD becomes a line

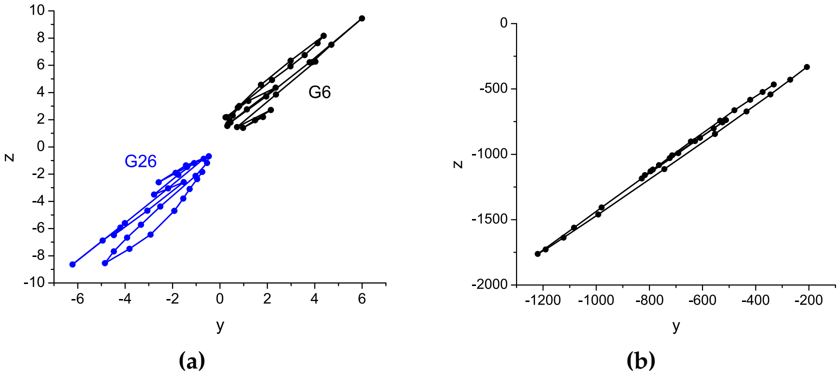

Figure 5.10: *(a) The xDNA curve of OVD1 in the G10 and G26 measurement geometry and (b) in Gn measurement geometry.*

with a 54° slope corresponding to aspecular angle of 45°. Thus, adding more geometries does not result in obtaining a more characteristic xDNA curve, but rather the opposite. G10 measuring geometry seems to provide an xDNA curve that is unique for a specific sample.

5.2.5 Examples of OVDs

In order to provide more evidence that G10 measurement geometry gives a unique and characteristic xDNA curve, we show here the goniospectrometric space curve in G6 measurement geometry for multiple OVDs along with the polar coordinate sRGB image using D65 illumination (Figs. 5.11–5.22).

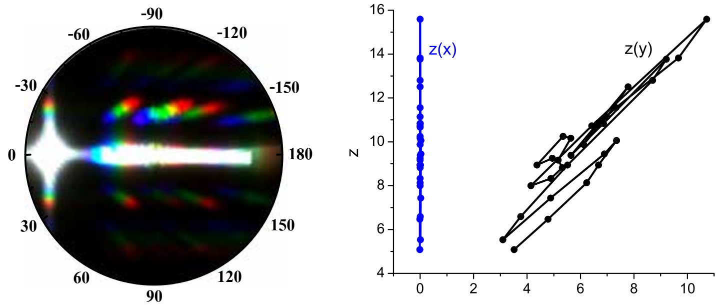

(a) **(b)**

Figure 5.11: *(a) The sRGB image and (b) xDNA graph in G10 measurement geometry of the OVD5.*

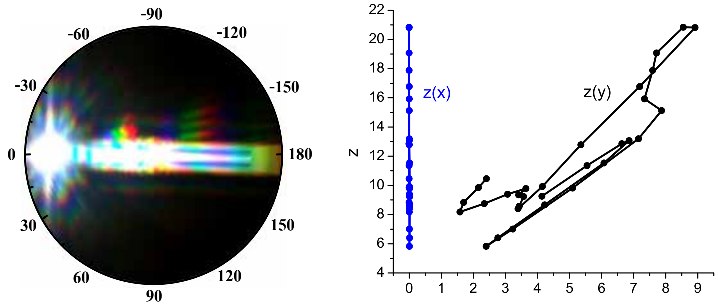

(a) **(b)**

Figure 5.12: *(a) The sRGB image and (b) xDNA graph in G10 measurement geometry of the OVD6.*

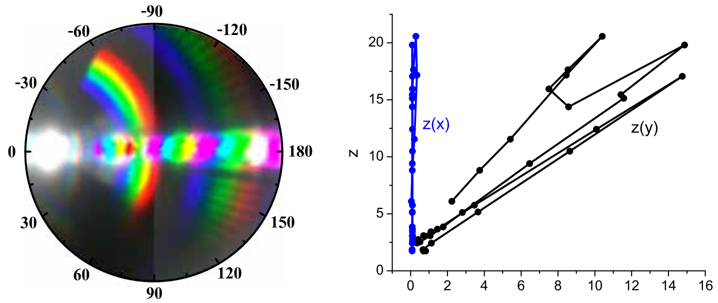

(a) **(b)**

Figure 5.13: *(a) The sRGB image and (b) xDNA graph in G10 measurement geometry of the OVD7.*

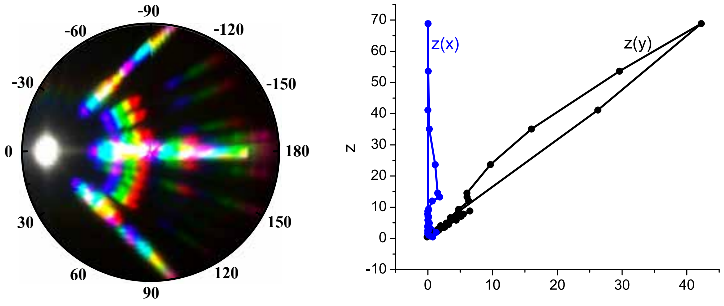

(a) (b)

Figure 5.14: *(a) The sRGB image and (b) xDNA graph in G10 measurement geometry of the OVD8.*

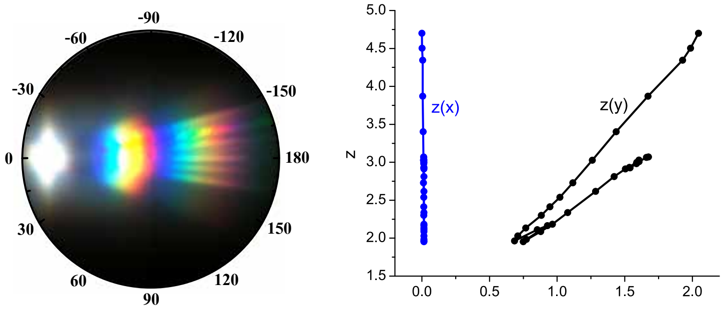

(a) (b)

Figure 5.15: *(a) The sRGB image and (b) xDNA graph in G10 measurement geometry of the OVD9.*

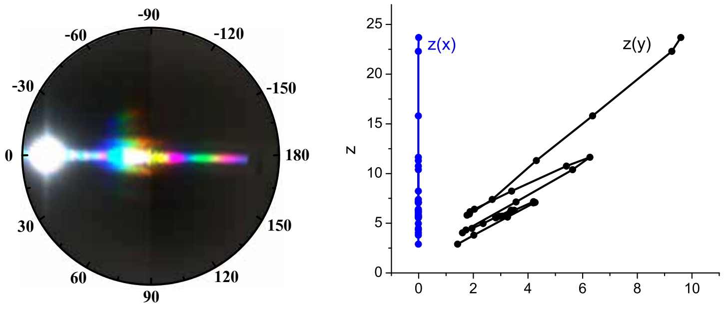

(a) (b)

Figure 5.16: *(a) The sRGB image and (b) xDNA graph in G10 measurement geometry of the OVD10.*

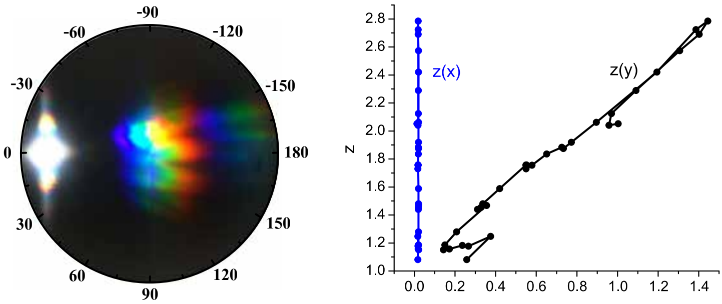

(a) **(b)**

Figure 5.17: *(a) The sRGB image and (b) xDNA graph in G10 measurement geometry of the OVD11.*

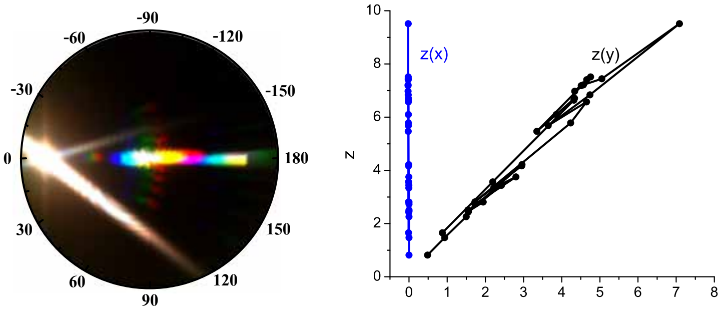

(a) **(b)**

Figure 5.18: *(a) The sRGB image and (b) xDNA graph in G10 measurement geometry of the OVD12.*

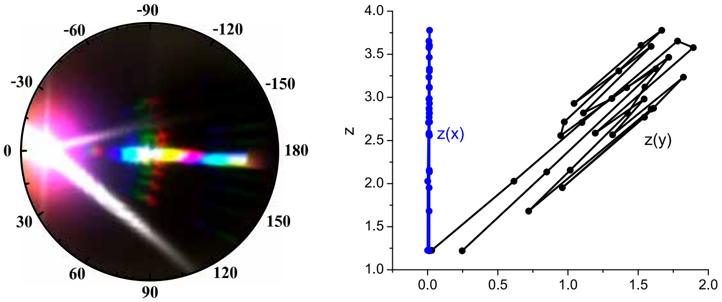

(a) **(b)**

Figure 5.19: *(a) The sRGB image and (b) xDNA graph in G10 measurement geometry of the OVD13.*

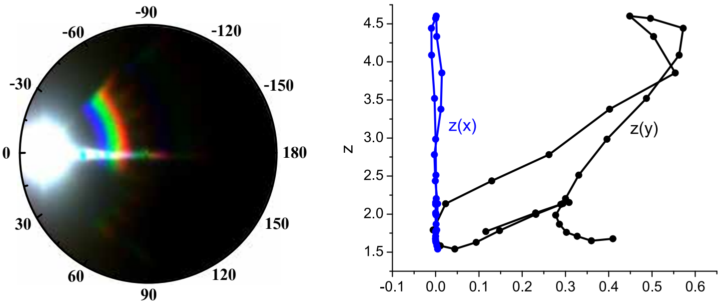

(a) **(b)**

Figure 5.20: *(a) The sRGB image and (b) xDNA graph in G10 measurement geometry of the OVD14.*

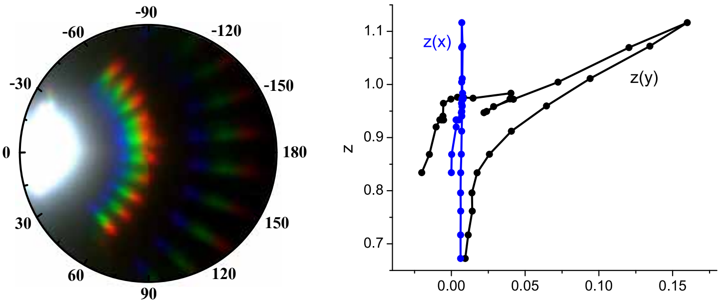

(a) **(b)**

Figure 5.21: *(a) The sRGB image and (b) xDNA graph in G10 measurement geometry of the OVD15.*

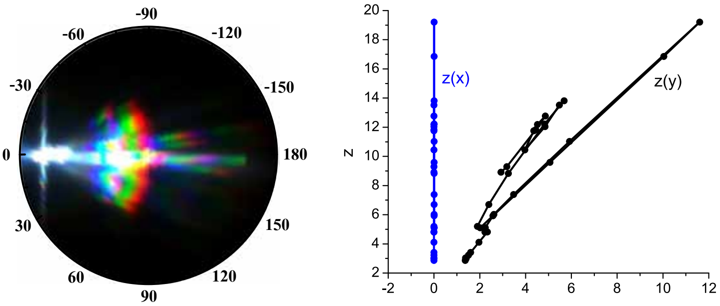

(a) **(b)**

Figure 5.22: *(a) The sRGB image and (b) xDNA graph in G10 measurement geometry of the OVD16.*

5.3 GONIOSPECTROMETRIC SPACE CURVE OF COATINGS WITH SPECIAL EFFECT PIGMENT

Coatings with special effect pigments are the subject of Paper **V** and Paper **VI**. The former introduces and evaluates the numerical model for calculating the reflectance spectra of such coatings. It also presents how the reflectance spectra are affected by different parameters of coatings with special effect pigments: surface coverage, mean flake tilt angle, standard deviation around that angle and the coating's substrate. Paper **VI** uses the numerical model to explore how the mentioned parameters affect the goniospectrometric space curve using three different types of special effect pigments.

The calculations for all coatings presented here were made for geometry G6 and using the Stokes vector of the incident light that of an unpolarized light (see Equation 4.3). The refractive indices of the coating's materials were obtained from the literature [46–48] in the spectral region 440–700 nm with 10 nm steps, because the published values for refractive index and absorption coefficient are limited to this region. The base coating parameters were set to $C = 1$, $\theta'_0 = 0$ and $\sigma' = 3$ (see Equation 4.21), which represents a coating fully covered by flakes, oriented parallel to the surface with 3° standard deviation of orientation. When and if any of these parameters deviate from the base values is specifically mentioned.

The comparison of modeled and measured reflectance factor is done in Paper **V**, using a coating with interference Iriodin 4504 pigments (see Figure 4 of Paper **V**), and in Paper **VI**, using a coating with metallic (M5) pigments and a coatings with layered (L5) pigments (see Figures 2 and 10 of Paper **VI**). The measured and calculated spectra show an acceptable match; the differences between the spectra could be a result of substituting optical constants of mica layer for optical constants of SiO_2, insufficient knowledge about the layers thicknesses, insufficient modeling of the roughness of the mica flakes or as a result of neglecting the scattering of light on the edges of flakes in the numerical model.

Paper **VI** uses calculated reflectance spectra for three types of special effect pigments; metal, transparent and layered ones. The materials and thicknesses of the coatings, needed for calculations, are compiled in Table 5.1; all coatings are assumed to have an aluminum substrate.

Table 5.1: *Basic data used for the studied coatings: the materials of flakes and the corresponding thickness used for calculations. The substrate in all three cases is aluminum and the binder is taken to be an acrylic pitch with thickness of 750 μm.*

	material(s)	thickness(es)
metallic (M5)	aluminum	2000 nm
transparent	TiO_2	200 nm
layered (L5)*	$Fe_2O_3/SiO_2/Fe_2O_3$	60.5/154/60.5 nm

* The flakes are described as layer/core/layer.

Metallic effect pigments act as a mirror; almost all light is reflected in the specular direction. Its reflectance is strongly dependent on the detection angle and only slightly on wavelength (see Figure 2a of Paper **VI**). Thus, the corresponding xDNA curve is a line with a very small span over y-axis (Fig. 5.23). Transparent effect pigments exhibit partial reflection of light on each boundary between the binder and the pigment with a larger refractive index. Nonetheless, the reflectance spectra's dependence on the detection angle is similar to that of the metallic effect pigments (see Figure 6a of Paper **VI**).A helix shaped xDNA curve, much longer than that for metallic coating, was obtained in the goniospectrometric space (Fig. 5.23). Layered effect pigments show interference due to a three-layer system with transparent SiO_2 core covered with a thin Fe_2O_3 layer on both sides (see Figure 10a of Paper **VI**). The xDNA curve of such a coating has a parabolic-like shape (Fig. 5.23).

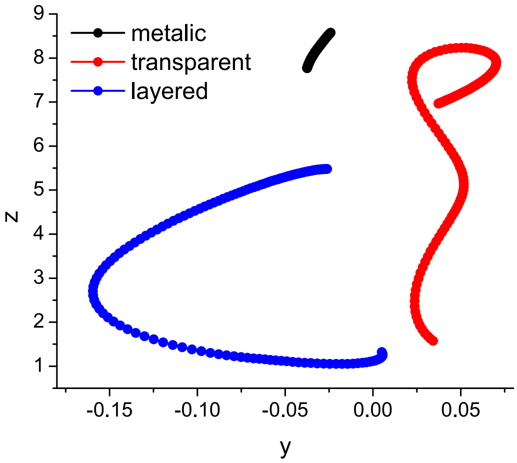

Figure 5.23: *xDNA curves for metallic, transparent and layered effect pigments. The calculation parameters for all three cases were* $C = 1$, $\theta'_0 = 0°$ *and* $\sigma' = 3°$. *The thickness of transparent pigments was 200 nm and layered pigments with* $Fe_2O_3/SiO_2/Fe_2O_3$ *structure had thicknesses of 60.5/154/60.5 nm.*

5.3.1 Influence of the mean flake tilt angle

When varying the mean flake tilt angle from -6° to 35° with respect to the sample surface, every reflected angle has its own reflectance peak, the position of which is directly related to the specular reflected angle. This can be seen both in Figure 8b of Paper **V** and in Figure 5b of Paper **VI**. We have to keep in mind that the refraction occurs at the binder-air interface, which causes a slightly nonlinear relation between the flake tilt angle and the reflected angle for the specular reflection on flakes (see Figure 8a of Paper **V**).

The goniospectrometric space curve behaves similarly when varying the mean flake tilt angle for all three special effect pigments types; it moves across the yz plane and rotates. xDNA curves for metallic, transparent and layered effect pigments differ from each other, as shown in Figure 5.23, but stay relatively the same inside their pigment type with varying θ'_0 (see Figures 5a, 8b and 12b of Paper **VI**). Figure 5.24 shows the xDNA points corresponding to

$\lambda = 650$ nm for varying θ_0' from -6° to 30° with 1° steps. The moving of the line is explained by the behavior of the reflectance spectra. From $\theta_0' = -6°$ to $\theta_0' = -3°$ the three near-specular angles increase, which results in a positive move along the z-axis, and no move in the y direction. Between $-3°$ and $6°$, the reflectance at $\theta_r = -60°$ rapidly diminishes; there is only a slight positive move in the z direction and a large positive move along the y-axis. From $6°$ to $19°$ the reflectance at $\theta_r = 0°$ is very important, which leads to a negative move of the xDNA curve along the z-axis and a small positive move in the y direction. Finally, in the region above 19°, the contribution of reflectance at $\theta_r = 30°$ and $\theta_r = 65°$ prevail, which causes a positive move along both axes. The rotation of the xDNA curves is shown only for a few selected θ_0' values for metallic effect pigments; xDNA curves for other θ_0' and pigment types behave similarly. The rotation is in the clockwise direction with an increased value of θ_0'; the effect is a consequence of different y-values obtained on both ends of the spectrum.

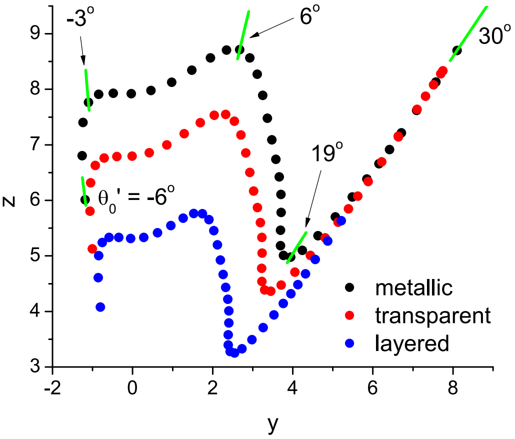

Figure 5.24: *Points in xDNA curves for wavelength 650 nm for metallic, transparent and layered effect pigments, for varying θ_0' from -6° to 30° with 1° steps. The green lines are full xDNA curves (for all wavelengths) for metallic effect pigments for θ_0' specified in the graph. Other parameters:* $C = 1$, $\sigma' = 3°$.

5.3.2 Influence of the flake orientation uniformity

Changing the uniformity of flake orientation (parameter σ') means going from an oriented structure appearing glossy, to a completely random structure having a matte appearance. The σ' was changed from 1° to 40° with 1° step; reflectance spectra for such a variation is shown in Figure 7 of Paper **V**. Near specular reflection angles have a quicker rise at small σ' and slowly converge to a constant at larger σ' values. The reflectance angles that are furthest from the specular direction, $\theta_r = 30°$ and $\theta_r = 65°$, do not have such a high reflectance as the other angles and also start to increase at larger σ'. This behavior is in accordance with the logistic distribution function that describes the flake orientation (see Equation 4.11); all reflected angles become possible when σ' is large enough.

As in the case of the θ'_0 variation, the xDNA curves for metallic, transparent and layered effect pigments behave similarly (see Figures 4a, 8a and 12a of Paper **VI**), thus only xDNA points for wavelength 650 nm are shown in Figure 5.25, along with some full xDNA curves for metallic effect pigments.

The move of the xDNA curves across the yz plane can be explained using three regions; (a) $1° < \sigma' < 3°$, (b) $3° < \sigma' < 16°$and (c) $\sigma' > 16°$. In region (a), reflectance angles closest to the specular direction show large changes ($\theta_r \leq -30°$), while other angles have negligible intensity. This results into a large positive move along the z-axis, and a small positive move in the y direction. In contrast, xDNA curves have a large positive move along the y-axis and smaller negative move in the z direction in region (b). This is caused by light increasingly reflecting away from the specular direction (θ_r >0°); the largest change occurs for θ_r =65°. In the third region, (c), the reflectance decreases for all angles except for θ_r =65°. This is shown in goniospectrometric space as a negative move along both the y- and z-axes. Simultaneously with the move of the xDNA curve, it also rotates through all the three regions; the effect is analogous as with the variation of θ'_0.

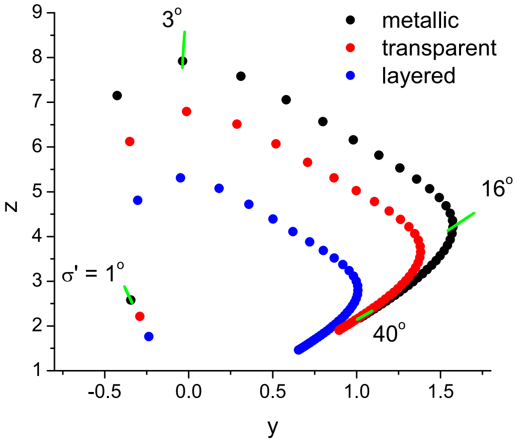

Figure 5.25: *Points in xDNA curves for wavelength 650 nm for metallic, transparent and layered effect pigments, for varying σ' from 1° to 40° with 1° steps. The green lines are full xDNA curves (for all wavelengths) for metallic effect pigments for σ' specified in the graph. Other parameters:* $C = 1$, $\theta'_0 = 0°$.

Effect of the flake orientation uniformity is also shown with measurements of two coatings with metal effect pigments, labeled here as M1 and M2 (Fig. 5.26). The measurements were done using the bidirectional spectrometer described in Paper **III**. The polar coordinate sRGB images using D65 illumination of the two coatings appear similar with the difference of M2 having an overall slightly lighter sRGB image. This is consistent with the orientation spread of the pigments; the M1 coating has pigments well-oriented, parallel to the coating surface, giving a glossy appearance with the highest intensity in the specular reflection and lower intensity at angles further away from the specular. In contrast, the M2 coating has randomly oriented pigments, which leads to a more matte appearance, in which all the reflected angles have roughly equal intensity. The xDNA curves for the M1 and M2 are shown in Figures 5.26c and 5.26d. M1 has smaller standard deviation, which leads to the xDNA curve having a higher z and lower y values than the xDNA curve for M2. This is in accordance with the theoretical predictions, illustrated in Figure 5.25. The contribution of off-plane measured angles is not large; thus, the xDNA curves have very small x values. The difference in the shape of the xDNA curves for M1 and M2 are very small and can probably be attributed to different pigment shapes and sizes.

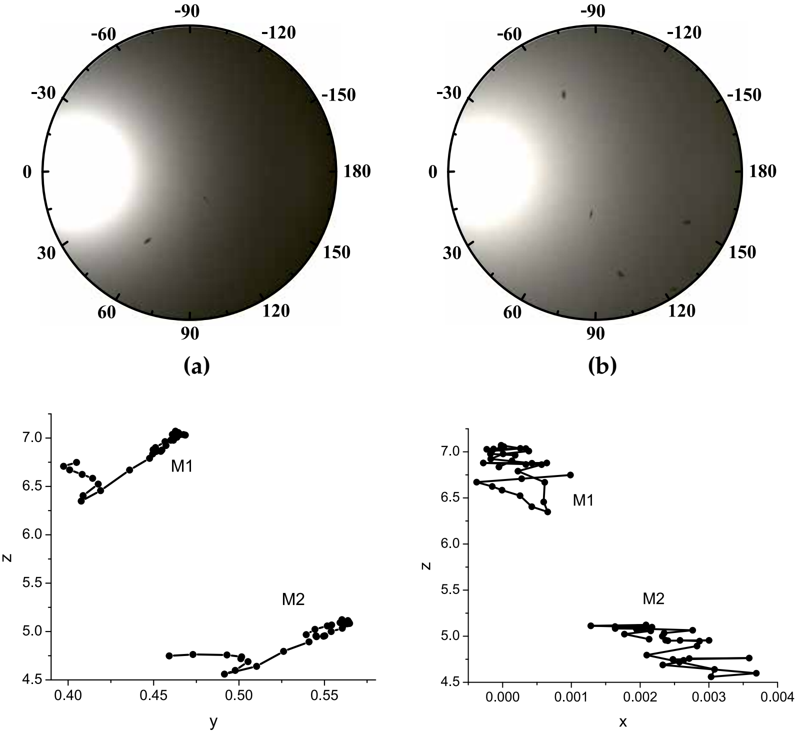

(a) (b)

(c) (d)

Figure 5.26: *The sRGB images for (a) M1 and (b) M2 coating with metal effect pigments, respectively. xDNA curves, obtained using G10 measurement geometry, for both coatings are shown as projections in (c) zy and (d) zx plane.*

5.3.3 Influence of the surface coverage

Surface coverage, denoted as parameter C, can be varied by changing the volume concentration of special effect pigments or their size.

Smaller surface coverage results in reflectance spectra being more affected by the coating's substrate; at small C values, the reflectance becomes similar to that of the substrate (see Figures 5, 9 and 10 of Paper **V**). For metallic, transparent and layered effect pigments, the goniospectrometric space curve moves towards larger y and z values when C is decreased. Simultaneously, it also rotates which is the same effect as observed for variations of θ'_0 and σ'. xDNA curves shorten and slowly transform into a line, characteristic for aluminum or white paper, depending on what the coating substrate is (see Figures 3b, 7 and 11 of Paper **VI**).

With decreasing C, the substrate plays an increasingly important role; the xDNA curve at $C = 0$ depends only on the coating substrate, since there are no more special effect pigments present in the coating. Thus, the choice of substrate is very relevant; this is shown in Figures 5.27 and 5.28, where a coating with layered effect pigments is applied to different color paper (white, black, magenta, cyan and yellow). The reflectance spectra of the substrates can be found in Figure 10 of Paper **V**.

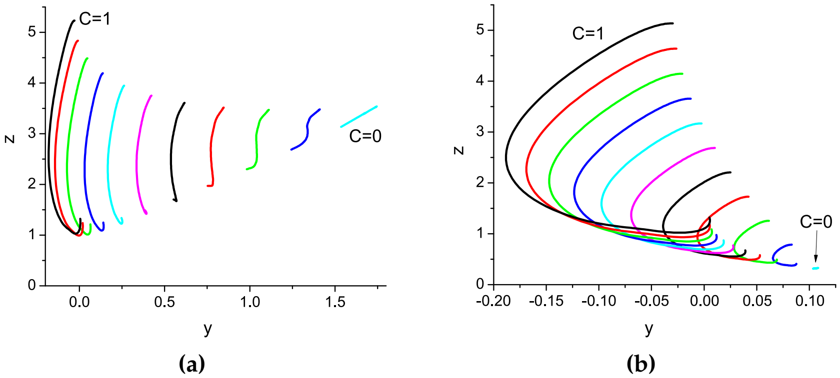

Figure 5.27: *xDNA curve for varying C from 1 to 0 with steps of 0.1 for coating with layered effect pigments applied on (a) white and (b) black paper. The reader should pay attention to different y scale of the two graphs (horizontal axis). The other calculation parameters are:* $\theta'_0 = 0°$ *and* $\sigma' = 3°$.

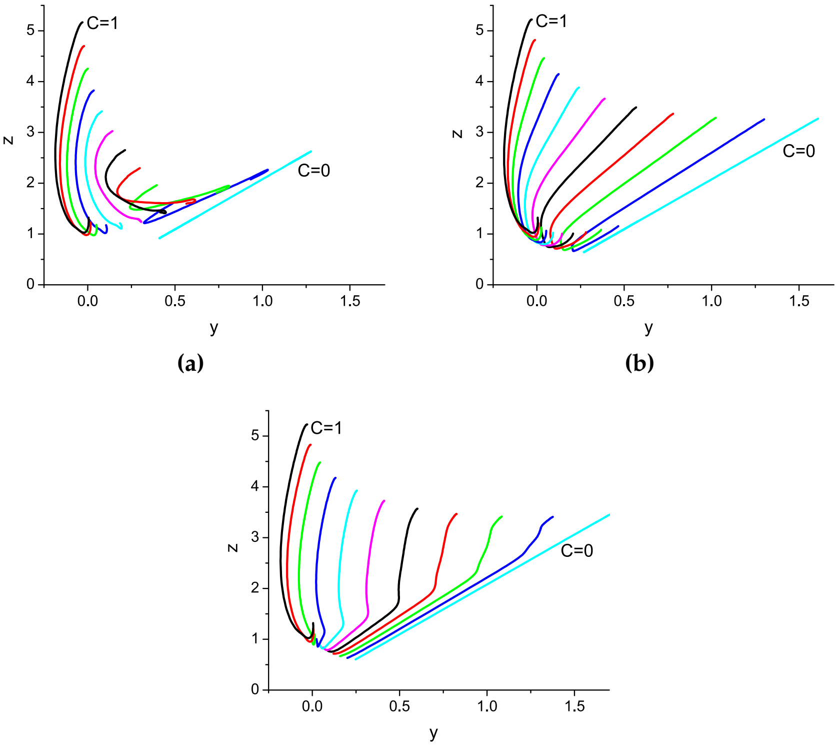

(a) (b) (c)

Figure 5.28: *(a) xDNA curve for varying C from 1 to 0 with steps of 0.1 for coating with layered effect pigments applied on cyan, (b) magenta and (c) yellow paper.*

5.3.4 Influence of flake's thickness

Changing the thickness of metallic effect pigments does not affect the goniospectrometric space curve, since the flakes reflect all incident light. However, the thickness has a great influence on coatings with transparent and layered effect pigments. The thickness for the former was changed in range from 20 to 500 nm; the change in reflectance spectra can be seen in Figure 9 of Paper **VI**. At smaller thicknesses, the spectra are more or less flat, showing no interference effect. When the thickness increases, the reflectance spectra develop an interference structure. Correspondingly, the xDNA curves change from a line at small thickness, to a helix-shaped xDNA curves, that have the number of loops equal to the number of interference peaks in spectra (Fig. 5.29).

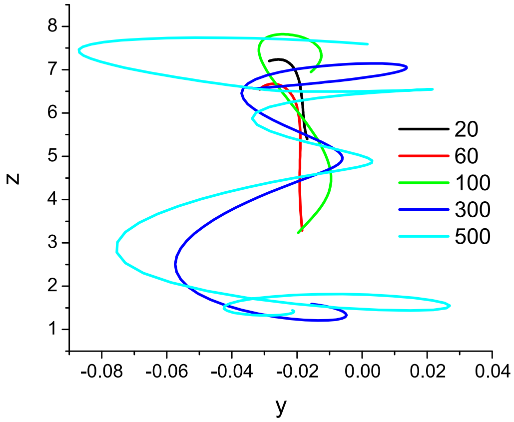

Figure 5.29: *xDNA curves of coatings with transparent effect pigments with varying thicknesses from 20 to 500 nm, as denoted in the legend in nm. Other calculation parameters are* $C = 1$, $\theta'_0 = 0°$, $\sigma' = 3°$.

Coatings with layered effect pigments have two options for varying the thickness; changing the thickness of the Fe_2O_3 layer at constant thickness of the transparent SiO_2 core and vice versa (Fig. 5.30). We again see the change from almost a line for a very small thickness, where there is no interference, to a loop-shaped xDNA curve for larger thicknesses, analogous as for coating with transparent effect pigments (see also Figures 13 and 14 of Paper **VI**). All examples of changing the pigment's thickness are in accordance with the previously shown interference layers (Figs. 5.2 and 5.3).

5.3.5 Comparison of colorimetricaly same coatings

Three colorimetricaly same coatings with metal effect pigments, denoted here as M3, M4 and M5, are compared in Figure 5.31. They were obtained from three different manufacturers but prepared for the same color shade. sRGB images of the three coatings (Figs. 5.31a–5.31c) are indeed very similar and can hardly be differenti-

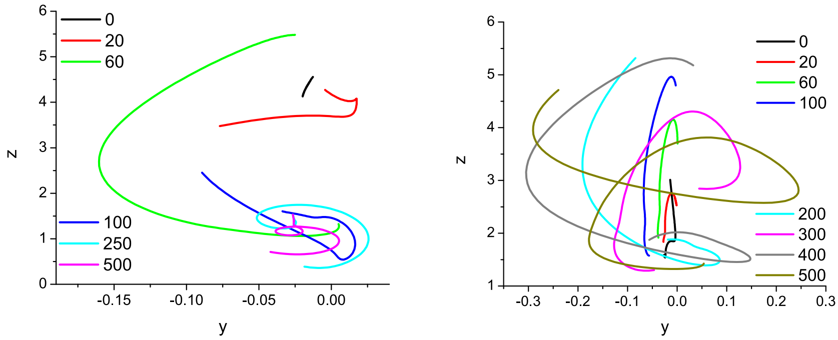

(a) **(b)**

Figure 5.30: *(a) xDNA curves of coatings with layered effect pigments with varying thickness of the Fe_2O_3 layer on the 154 nm thick SiO_2 core and (b) having different thicknesses of the SiO_2 core and a 60.5 nm thick Fe_2O_3 layer. The thicknesses are denoted in legends in nm. The other calculation parameters are $C = 1$, $\theta_0' = 0°$, $\sigma' = 3°$.*

ated. However, if we observe the xDNA curves of M3–M5, the difference is clearly seen; M3 and M4 have pigments with similar size and shape, with rough edges, which results in a similar position of the xDNA curve. Coating M5, however, has pigments with different sizes and shapes with smooth edges (compared to those in M3 and M4); thus, the xDNA curve position is at larger x, y and z values.

When we compare the xDNA curves of M3–M5 with the xDNA curves obtained using numerical model, we can assume that all three coatings have the same surface coverage (parameter C); the change in the xDNA curve position can be attributed to different mean flake tilt angle values, θ_0' (compare Figs. 5.31d and 5.24). The xDNA curves of the three coatings, M3–M5, should also be compared with coatings M1 and M2 (Figs. 5.26c and 5.26d), since all the coatings have the same type of pigments. Indeed, all the xDNA curves are almost line-shaped, with very small spans in x direction.

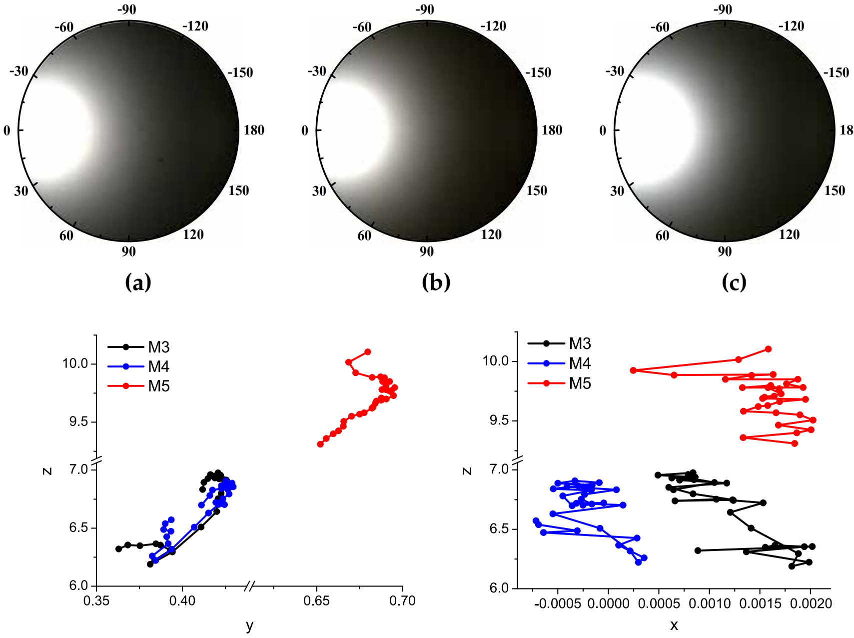

(a) (b) (c)

(d) (e)

Figure 5.31: *The sRGB images and SEM images for (a), (d) M3, (b), (e) M4, and (c), (f) M5 coating with metal effect pigments, respectively. xDNA curves, obtained using G10 measurement geometry, for all three coatings are shown as projections in (g) zy and (h) zx plane.*

5.3.6 Coatings with cover layer

Figures 5.32–5.36 show the xDNA curves of L-set coatings with and without the cover layers, along with sRGB images. The reader can observe different shapes of the xDNA curves for different types of layered effect pigments. What all graphs exhibit, is the translation towards smaller z values of the xDNA curves for coatings with cover layers. This can be explained by the smaller reflectance values in the angles near specular reflection. The same effect can also be seen on the sRGB images; the coatings with cover layers have a smaller light spread around the specular reflection at $\theta_r = 45^\circ$ and $\phi_r = 0^\circ$. All coatings also have the sRGB images symmetric along the $\phi_r = 0/180^\circ$; this results in the x coordinate of xDNA graphs to be practically zero.

Coatings with cover layers present a challenge for optical devices that are currently used for measurements; optical microscope, integrating sphere and scanning electron microscope (SEM). Because of the additional layer, the pigments are situated too far below the surface of the coating, making measurements taken with optical microscopes unusable. In contrast, diffuse reflectance measurements with integrating sphere can measure coatings with a cover layer but only with increased measurement errors. Diffuse reflectance measurements measures all the reflected light from the sample with an integrating sphere that usually has a small opening area. Thus, a part of the reflected light misses the opening because the cover layer scatters the light reflected at large angles away from it. The thicker cover layer and smaller opening area result in larger measuring errors; this is the so-called aperture error, taking place at rough and optically complex samples. SEM measurements require the etching of the coating's surface prior to the measuring. This is problematic for all coatings, regardless of the cover layer, since the sample is destroyed during the measurement process. Furthermore, coatings with a cover layer require significantly longer etching times in order to reach the area of the coating with pigments. For this reasons, a highly selective etching procedure has to be selected, such as weakly ionized oxygen plasma [42]. Goniospectrometric space, presented in this study, is not only capable of measuring coatings with cover layers but is also able to distinguish between the coatings with and without the cover layers.

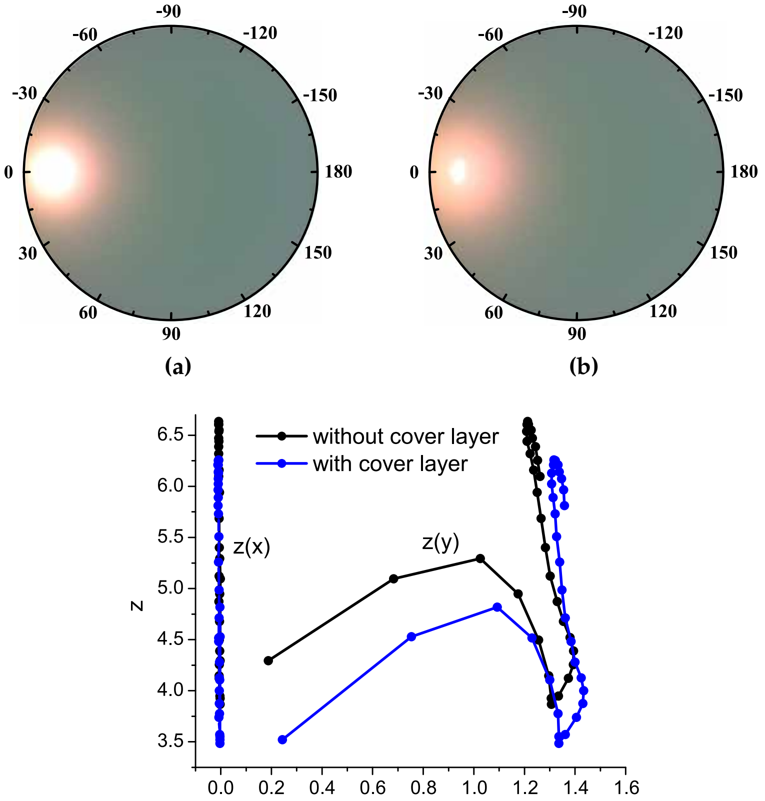

(a)

(b)

(c)

Figure 5.32: *The sRGB image of (a) L1 without cover layer and (b) L1 with cover layer. (c) xDNA curves for L1 with and without the cover layer, using the G10 measurement geometry.*

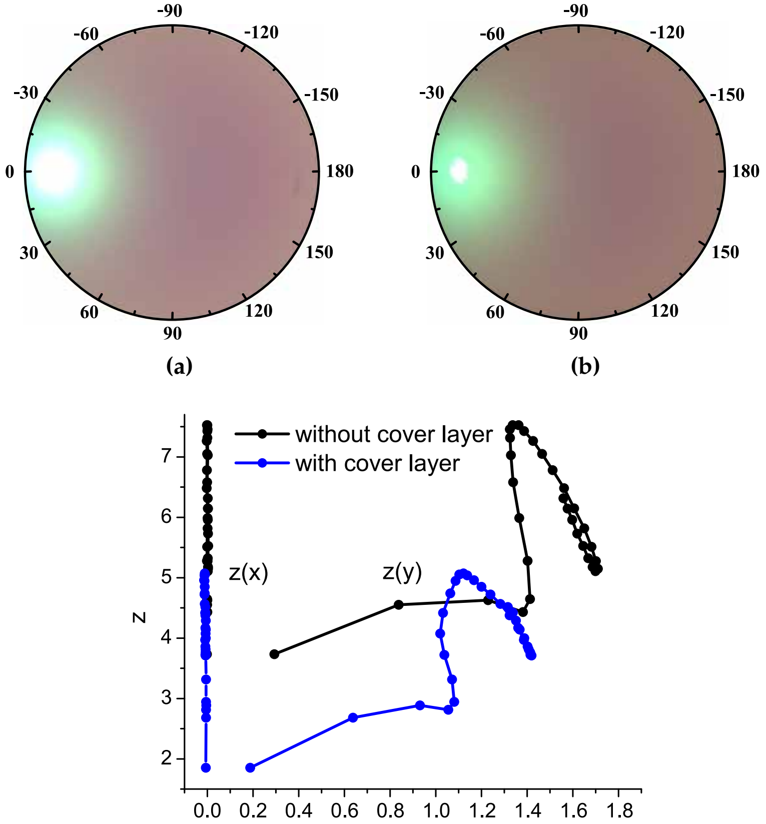

(a)

(b)

(c)

Figure 5.33: *The sRGB image of (a) L2 without cover layer and (b) L2 with cover layer. (c) xDNA curves for L2 with and without the cover layer, using the G10 measurement geometry.*

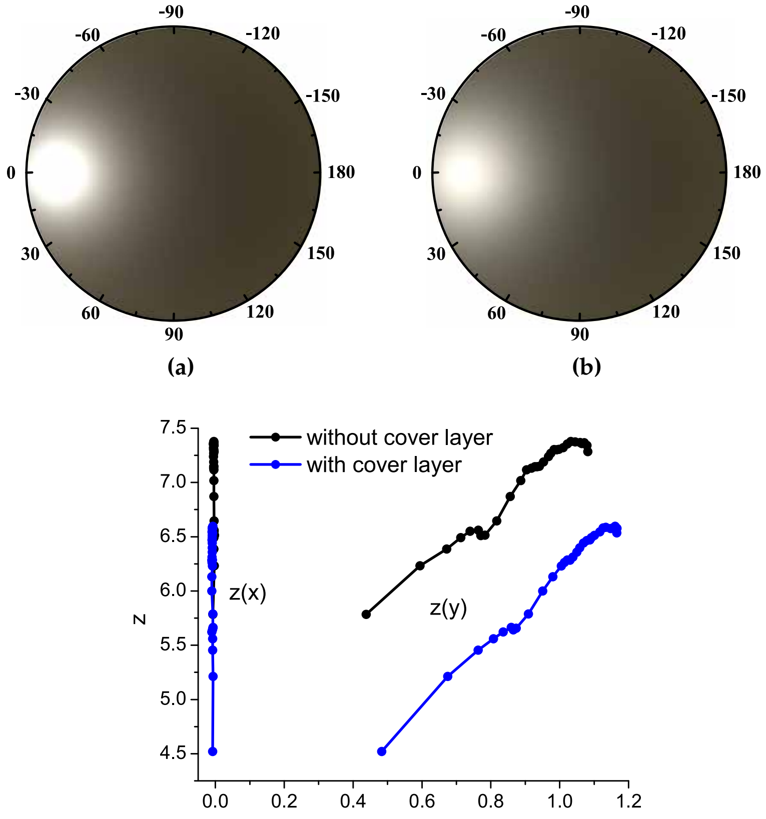

(a) (b)

(c)

Figure 5.34: *The sRGB image of (a) L3 without cover layer and (b) L3 with cover layer. (c) xDNA curves for L3 with and without the cover layer, using the G10 measurement geometry.*

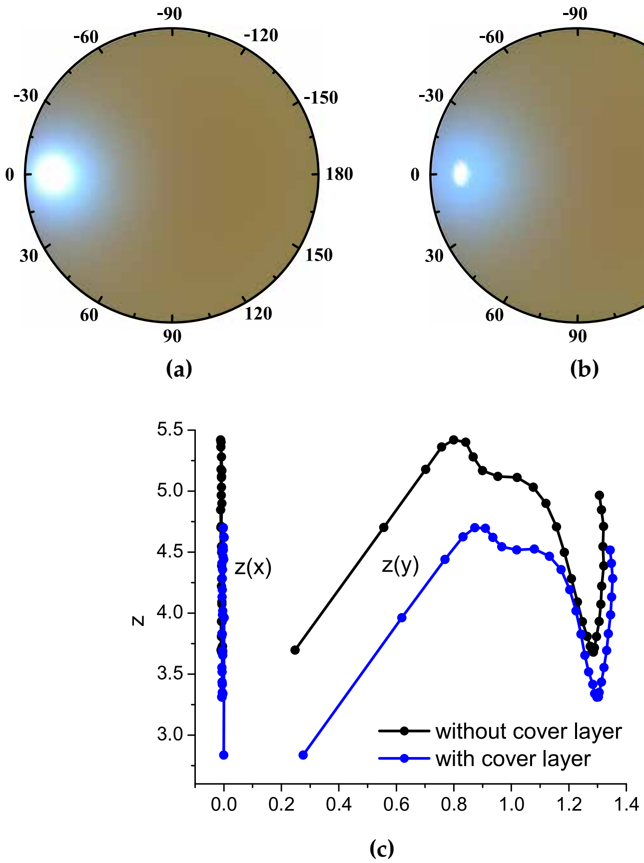

(a) (b)

(c)

Figure 5.35: *The sRGB image of (a) L4 without cover layer and (b) L4 with cover layer. (c) xDNA curves for L4 with and without the cover layer, using the G10 measurement geometry.*

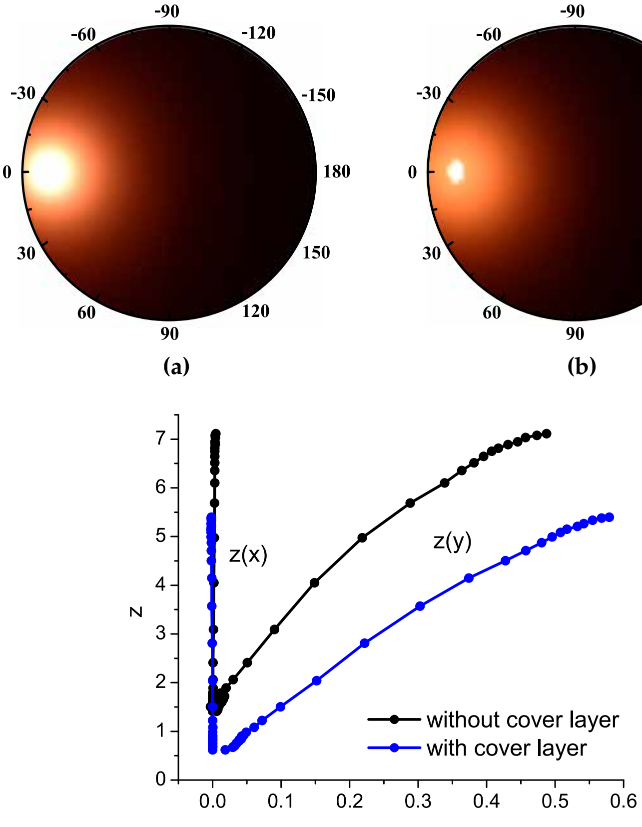

(a) (b)

(c)

Figure 5.36: *The sRGB image of (a) L5 without cover layer and (b) L5 with cover layer. (c) xDNA curves for L5 with and without the cover layer, using the G10 measurement geometry.*

5.3.7 More examples of coatings with special effect pigments

Figures 5.37–5.52 show xDNA curves for T-set coatings along with sRGB images under D65 illumination. Even though the special effect pigments used in these coatings have very similar specifications, they are clearly identifiable using xDNA curves.

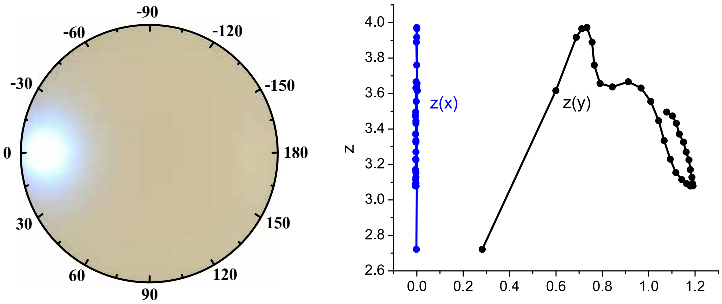

(a) (b)

Figure 5.37: *(a) The sRGB image and (b) xDNA graph in G10 measurement geometry of the T1.*

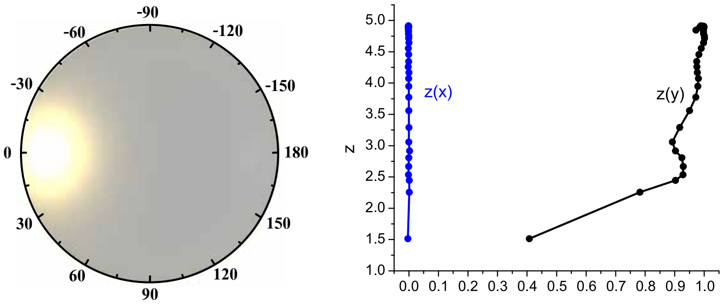

(a) (b)

Figure 5.38: *(a) The sRGB image and (b) xDNA graph in G10 measurement geometry of the T2.*

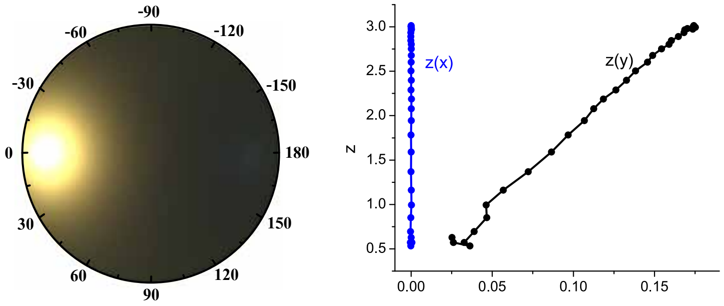

(a) **(b)**

Figure 5.39: *(a) The sRGB image and (b) xDNA graph in G10 measurement geometry of the T3.*

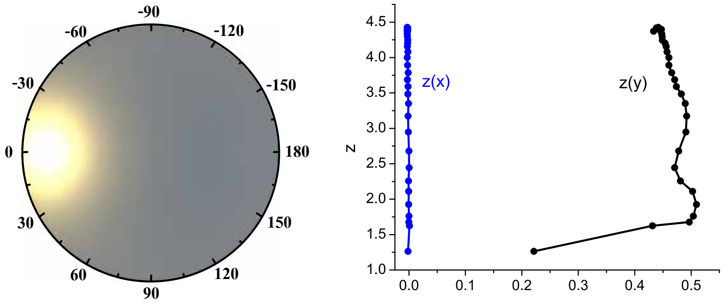

(a) **(b)**

Figure 5.40: *(a) The sRGB image and (b) xDNA graph in G10 measurement geometry of the T4.*

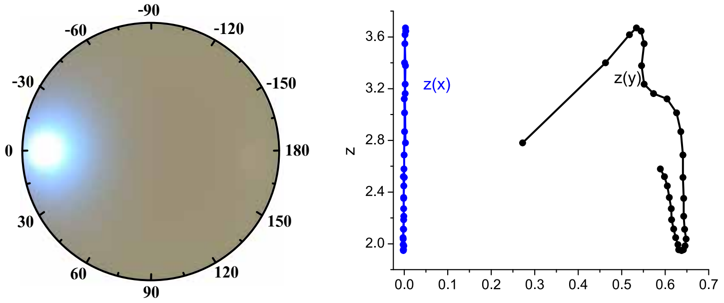

(a) **(b)**

Figure 5.41: *(a) The sRGB image and (b) xDNA graph in G10 measurement geometry of the T5.*

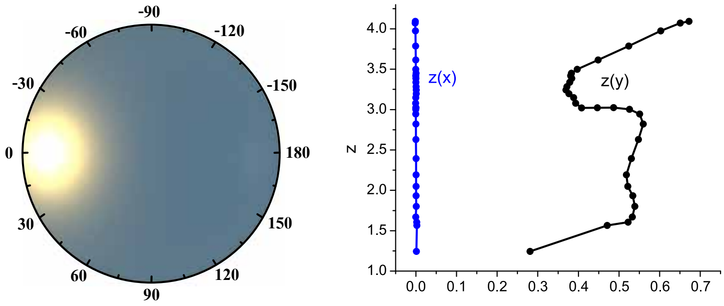

(a) **(b)**

Figure 5.42: *(a) The sRGB image and (b) xDNA graph in G10 measurement geometry of the T6.*

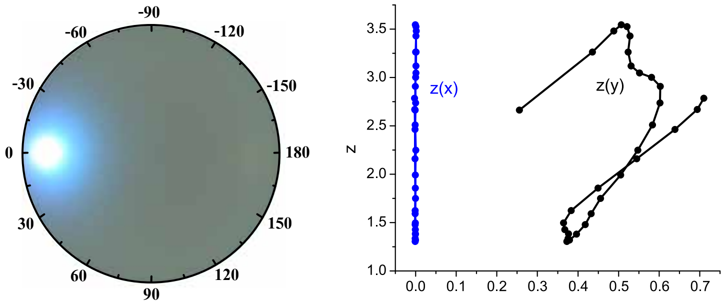

(a) **(b)**

Figure 5.43: *(a) The sRGB image and (b) xDNA graph in G10 measurement geometry of the T7.*

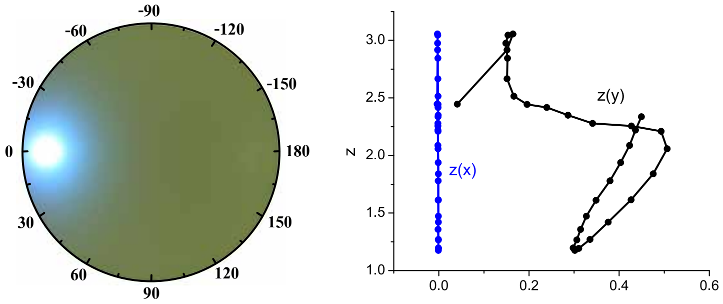

(a) **(b)**

Figure 5.44: *(a) The sRGB image and (b) xDNA graph in G10 measurement geometry of the T8.*

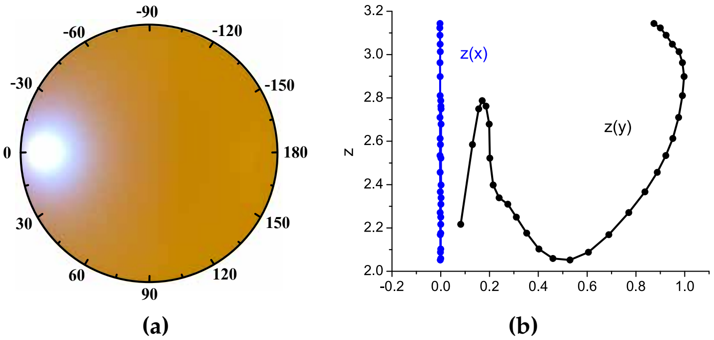

Figure 5.45: *(a) The sRGB image and (b) xDNA graph in G10 measurement geometry of the T9.*

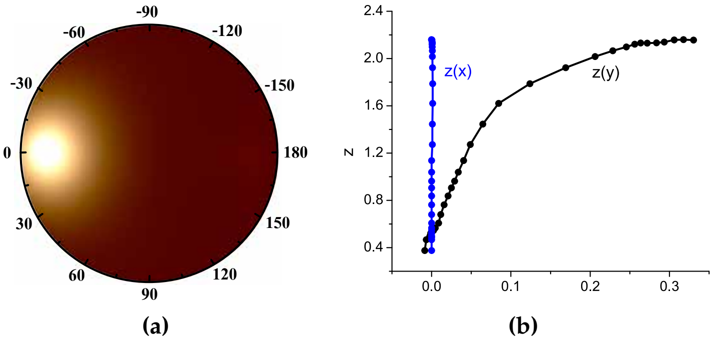

Figure 5.46: *(a) The sRGB image and (b) xDNA graph in G10 measurement geometry of the T10.*

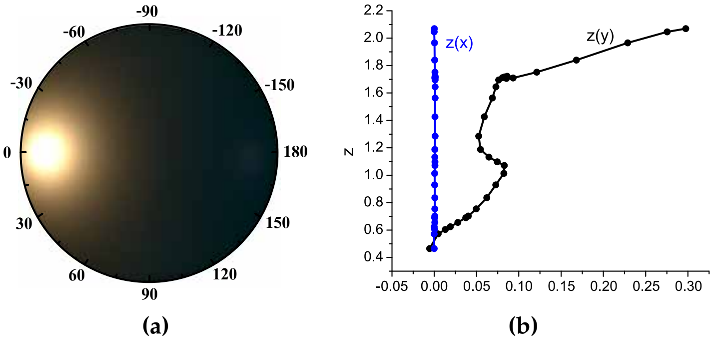

Figure 5.47: *(a) The sRGB image and (b) xDNA graph in G10 measurement geometry of the T11.*

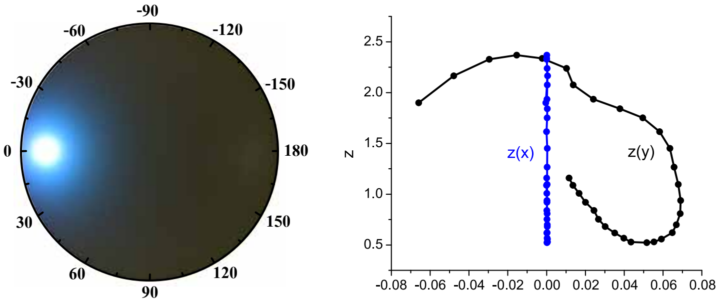

(a) **(b)**

Figure 5.48: *(a) The sRGB image and (b) xDNA graph in G10 measurement geometry of the T12.*

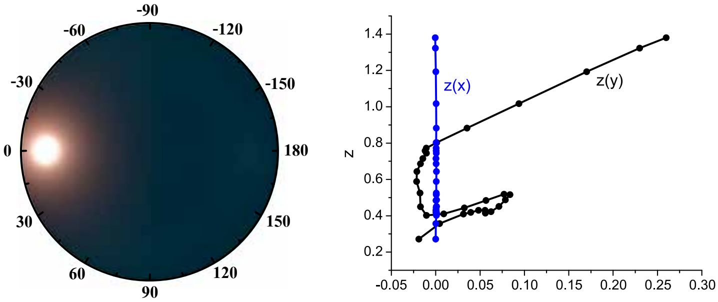

(a) **(b)**

Figure 5.49: *(a) The sRGB image and (b) xDNA graph in G10 measurement geometry of the T13.*

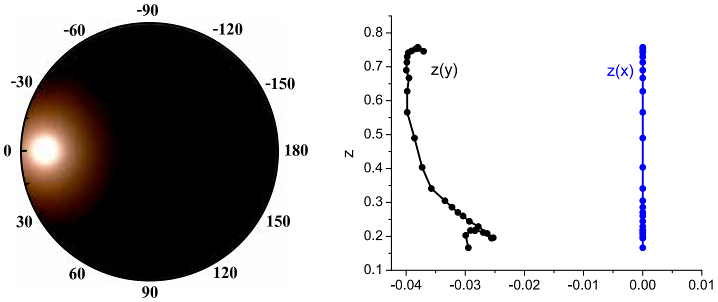

(a) **(b)**

Figure 5.50: *(a) The sRGB image and (b) xDNA graph in G10 measurement geometry of the T14.*

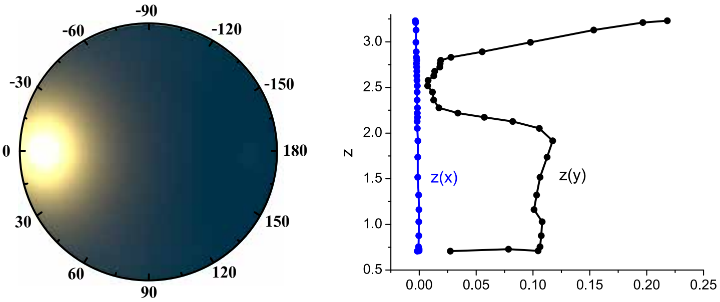

(a) **(b)**

Figure 5.51: *(a) The sRGB image and (b) xDNA graph in G10 measurement geometry of the T15.*

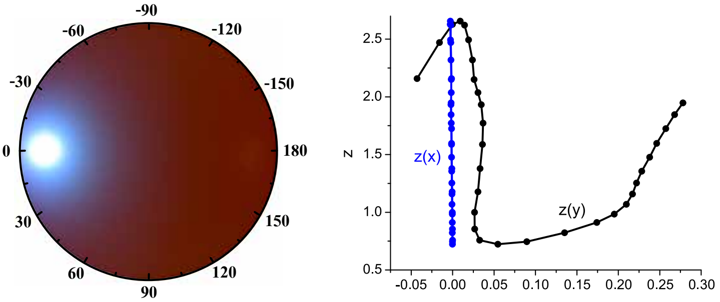

(a) **(b)**

Figure 5.52: *(a) The sRGB image and (b) xDNA graph in G10 measurement geometry of the T16.*

The type and thickness of the applied flakes in a coating define the characteristic shape of the xDNA curve. Moreover, the xDNA curve's location, length and orientation depends on the coating parameters: surface coverage of flakes, their orientation and orientation distribution, and also the type of coating substrate. The G10 geometry was shown to be sufficient to distinguish angular dependent optical properties of different coating. For coatings with flakes oriented mostly parallel to the surface, even G6 geometry could be used. This is a result of a smooth angular distribution of the reflectance spectra.

6 Discussion, conclusions and future work

6.1 DISSCUSSION

This study analyzed optically complex samples using goniospectrometric measurements and numerical modeling of their reflectance. Under-sampled BRDF, measured and modeled, was transformed into an sRGB image and goniospectrometric space. One of the questions of the thesis was whether the goniospectrometric space curve can be regarded as an appearance fingerprint of optically complex samples.

The goniospectrometric space curve of optically known samples was analyzed first (Paper **I**); reflectance spectra using measurement geometry G19 with two illumination angles were transformed to xDNA curves of various bulk samples and sub-micron layers. Polished silicon wafer and black cardboard both have their xDNA curves restricted almost to a point, but are located at very different coordinates in the goniospectrometric space. An unpolished silicon surface has a line-shaped curve that spreads in three dimensions when the contribution of off-plane reflections becomes larger. Similarly, the glossy and matte sides of the paper also transform into a line-shaped xDNA curve. However, the length of the xDNA line gets longer for the glossy surface of paper, while the dependence is the opposite for unpolished silicon wafers. xDNA curves also reveal the difference between surface and volume reflection, characteristic for silicon wafer and paper, respectively.

Interference layers were analyzed using thin layers of silicon nitride and submicron varnish layers on a paper substrate. In both cases, the xDNA curves were ellipsoidal loops, with the number of loops corresponding to the number of interference fringes in reflectance spectra. The goniospectrometric space curves of varnish layers were also influenced by the substrate; the xDNA curve of a layer on white paper has a line characteristic for white paper, and a loop, characteristic for the interference layer.

Pigmented coatings that act by absorption and scattering also have line-shaped xDNA curves. The spectral features giving rise to color do not produce a loop characteristic for interference fringes, but an almost flat curl parallel to the rest of the line. The length of the individual xDNA curve increases with layer thickness, which shows increased surface gloss. The difference in layer thickness was observed as a displacement between individual xDNA curves.

Paper **II** and Paper **IV** analyzed the calculated BRDF of diffraction gratings having parallel sinusoidal grooves with periods between 0.35 and 5 μm and amplitudes below 0.2 μm, using G6 geometry. The goniospectrometric space curves of these diffraction gratings, transformed from calculated BRDF, consist of straight lines and possible interconnections. The lines are a result of spectrally isolated diffractions and interconnections arise when some of the diffractions partially overlap. The slope of the xDNA lines depends on the aspecular angle, which could enable detecting the grating period of the unknown diffraction grating.

Both Paper **II** and Paper **IV** analyzed the spectral and angular resolution needed in order for the goniospectrometric space curve to provide a unique appearance fingerprint of the sample; the former using only diffraction gratings, and the latter also using optically variable devices (OVDs). Paper **II** deals with the resolution question theoretically, while Paper **IV** uses goniospectrometric measurements obtained with a bidirectional spectrometer described in Paper **III**. Both papers show that the 10 nm wavelength step is sufficiently large enough to measure all diffractions. The angular resolution was tested by adding more measuring geometries; this resulted in the detection of more diffractions and, consequently, more interconnections in the xDNA curves. Hence, more geometries do not produce a better fingerprint but rather blur the simplified characteristic image. The G10 measurement geometry is regarded as being optimal for a unique appearance fingerprint of a sample. Since diffraction gratings and OVDs contain the strongest spectral and angular effects, the mentioned resolutions apply also for other samples as well (coatings with special effect pigments).

Paper **V** presented a numerical model for coatings with special effect pigments, and it analyzed how the reflectance spectra changed with different coating parameters, using measurement geometry G6. The obtained results were then used in Paper **VI**, where coatings with three types of flakes were analyzed, applying metallic, transparent and layered effect pigments. Goniospectrometric space curves for these three types of coatings are a line, a closed loop and parabolic shapes, respectively. The location, length and orientation of the xDNA curve for coating with special effect pigments depends on the other parameters of the coating: the surface area covered by flakes, their orientation and uniformity of orientation.

The results of this study prove the xDNA evaluation procedures, according to which it is stated that each coating is described by a specific xDNA curve and they can be compared accordingly. Translations, alignment and scaling of the curves are applied in these procedures, which is attributed to variations of the coating thickness, different drying conditions (which influences the orientation of flakes) and the particle size distribution of flakes inside coatings, respectively. Indeed, the changes in coating parameters resulted in translation, alignment (rotation) and scaling (changing size) of the xDNA curve. The changes also included the differences in the coating recipe (different pigment types and different pigment thicknesses). Thus, the goniospectrometric space curve contains all features of the angular dependent optical properties of coatings with special effect pigments.

Paper **III** introduced another way of presenting the BRDF; an sRGB image using D65 illumination. It included reflectance spectra for angular steps over all azimuthal angles at polar angles up to 60° with a 2° angular steps for both directions.

The sRGB images of coatings with special effect pigments have a smooth angular dependence, showing both specular and diffuse reflection, and are symmetric across the azimuthal line 0°/180°. Diffraction gratings also show specular and diffuse reflections, but have much more complex sRGB presentations. Measurements were done with grating's grooves perpendicular to the plane of incident; diffraction orders form the central line in the sRGB image showing a full spectrum of colors. Reflective and semitransparent gratings show equal diffraction orders while the background of semitransparent overlays can be observed in regions of the sRGB image where no diffraction occurs. The effects of all included optical features of OVDs are shown in their sRGB images; diffractions across the central line are the most frequently observed in sRGB images of OVDs. In contrast with sRGB images of diffraction gratings, the sRGB images of OVDs often have smudges in the central line, indicating several different grating periods. OVDs that have optical features with higher complexity show more complex effects in the sRGB images.

The sRGB images of coatings with special effect pigments are a good visual aid, but are generally not the optimum presentation of the samples. In contrast, the sRGB images of diffraction gratings and OVDs present the corresponding optical properties in sufficient details. However, the bidirectional reflection measurements over the entire hemisphere needed for the sRGB image, are long-lasting. For practical purposes, shorter measuring times and the usage of portable equipment is required. The goniospectrometric space curve, obtained using only G10 measurement geometry, can be considered to be a quick and effective solution to presenting the appearance of a sample. This was proven since all the samples in this study could be distinguished with the xDNA curve. Therefore, the goniospectrometric space curve using measurement geometry G10 can be regarded as a basic appearance fingerprint of optically complex samples.

6.2 CONCLUSIONS

This study provided theoretical analysis of diffraction gratings and simple OVDs using diffraction theory. It continued with an extended numerical model for coatings with special effect pigments. The three types of samples (diffraction gratings, OVDs, and coatings with special effect pigments) required BRDF measurements; for this purpose a bidirectional spectrometer was built and evaluated. The challenge of presenting the measured BRDF was overcome by using a polar coordinate sRGB image (D65 illumination). BRDF measurements and calculations were also transformed into a goniospectrometric space. Obtained xDNA curve was analyzed for all three types of samples. It was found that the optically complex samples can be observed and verified using the spatially undersampled BRDF presented by the xDNA curve. The study also showed that even the smaller number of geometries, G10, with a 10 nm wavelength step, can produce distinguishable xDNA curves. Contrary, large number of measurement geometries reduces the identifying properties.

The spectral and spatial resolution required to obtain a representative optical fingerprint (xDNA curve) can be achieved by handheld spectrometers. This is especially important for diffraction gratings and OVDs; the method could be used as an identification step while checking for counterfeits, without damaging the sample. The angular resolution can also be achieved by some handheld multi-angle spectrometers. This means that there is no need for additional measurement geometries; 6 in-plane and 4 off-plane angles suffice. Nevertheless, when introducing new samples (new type of flakes in coatings with special effect pigments, or new design of OVDs), it would be useful to measure the sample once with a bidirectional spectrometer in order to obtain the full BRDF data. By doing so, one could confirm that no important optical characteristics are missed when using G10 measurement geometry.

6.3 FUTURE WORK

Two general ways of extending this research could be mentioned, one considering the measurements and another the interesting gonioapparent samples.

Measurements were restricted in this work to 45° incidence angle, which was used in the bidirectional spectrometer and in the handheld multi-angle spectrometer. However, the former has the possibility to adjust the incident angle between 0° and 60° and the later has the possibility of applying also the near-normal incidence, 15°. Furthermore, if some more sophisticated spectrometer would be available, even more measuring geometries would be provided. Such a possibility is the Zeiss GK/311M spectrometer which provides illumination and detection angle with step size of 5°, giving about 220 measuring geometries. These possibilities were not taken into account here or were not available. It was regarded that majority of important properties are obtained by taking into account the most common incident angle, 45°. However, there are several attempts to analyze other illumination possibilities, among them a near-normal one ($< 20°$) and as large as possible (60° would be enabled by the bidirectional spectrometer).

Another idea would be the application of broader spectral range for BRDF measurements, outside of visible range. It is worth pointing out that some security features apply also the near infrared region to increase protection against forgery. Another need for the near infrared region seem to be solar applications; the sunlight's spectral region spreads from about 300 nm up to 2500 nm where only 43% is the visible light. Here, the visual effects are not very important but the interaction of a surface with the incident flux play the central role. Most research on this area made from the optics/radiometry is missing and would be welcome. It could be considered as a continuation of this study.

The coatings available for this study did not contain more complex flakes such as diffractive or liquid crystal-based pigments. Such pigments are known from the literature [35,38]. In these examples, layered flakes are applied, where one of the layer is diffraction grating or polymer with chiral cholesteric liquid crystal structure, respectively. However, during this study, no such sample was available. If such samples would be considered, the numerical model should be extended to enable diffraction effects and selective reflection according to the pitch of the liquid crystal structure. Furthermore, the temperature dependent effects should be taken into account for coatings with liquid crystal-based flakes.

Considering samples of coatings with special effect pigments, we should also mention the flakes orientation. We did not have the means of producing the coatings by ourselves; samples were taken from color card of effect pigments (Merck), provided by Helios (Slovenia) or by Tikkurila (Finland). Limited data were available for these samples, some of them were analyzed by chemical analytical methods to get the necessary data needed for numerical model. Main problem of the coatings samples, was the fact that all of them have flakes oriented parallel to the coating surface, except one (M2) that was prepared with more randomly oriented metallic flakes. Although coatings with other tilt angles are rare, some technological processes enable orientation of the flakes at other angles with reasonably narrow distribution. Moreover, the diffraction pigments could also be oriented according to the grooves [49]. Such samples are now an exception, but might become important in the future. Therefore, any research for the optical characterization would be welcome.

A Photographs of optically variable devices

This appendix contains the photographs of the optically variable devices (OVDs) used in this study, along with their description.

Figure A.1: *Photograph of (left) OVD1 and (right) OVD2.*

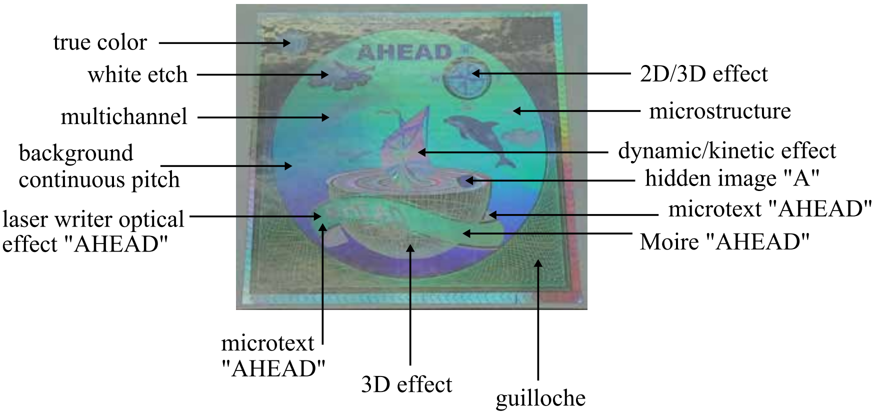

Figure A.2: *Photograph of OVD3 with labeled security features, taken from [30] (Figure A.1)*

Figure A.3: *Photograph of OVD4, taken from [30] (Figure A.14). It is a see-through diffractive interferential optically variable image structure, laminated over the portrait of an identification card. There is a color-shifting effect from transparent to green. The OVD4 was also photographed with the Handy Viewer that has left-handed and right-handed circular polarizers in the left and right openings, respectively. The sample is fully transparent through the left opening, while diffractive and interference effects are seen through the right opening.*

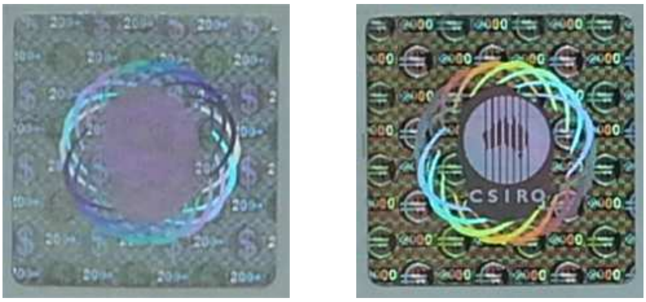

Figure A.4: *Photograph of OVD5 under two different viewing angles. It is an Exelgram taken from [30] (Figure A.2) made with electron beam lithography. Features found here are small lettering, logos, linear and translational traffic light effects, moving kinematic microtext and so-called two-channel effects.*

Figure A.5: *Photograph of OVD6 under three different viewing angles. It is a Vectorgram taken from [30] (Figure A.3) made with electron beam lithography. It consists of an array of pixels in which each pixel contains two or more subpixels with different optical effects.*

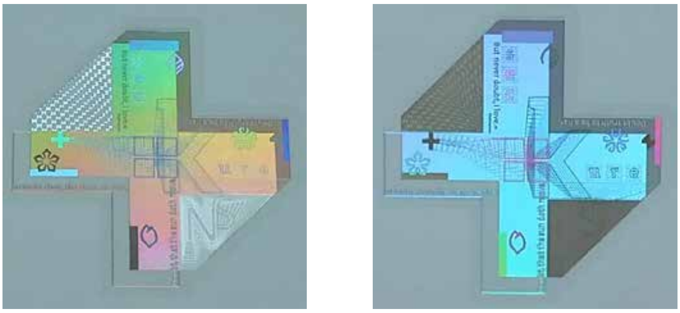

Figure A.6: *Photograph of OVD7 under two different viewing angles. It is a Kinegram security device taken from [30] (Figure A.4). It consists of effects such as diffractive watermark, dynamic transformations, asymmetric morphing, dynamic achromatic and nanotext.*

Figure A.7: *Photograph of OVD8 under three different viewing angles. It is a Kinegram Secure Memory Card taken from [30] (Figure A.5). It allows straightforward first-line visual authentication.*

Figure A.8: *Photograph of OVD9 under two different viewing angles. It is a Varimatrix hologram taken from [30] (Figure A.7). Optical effects include multiresolution SecureText, microtext and 3D background.*

Figure A.9: *Photograph of OVD10 under two different viewing angles. It is a HiMax OVD taken from [30] (Figure A.8) that consists of diffraction gratings with a width of 200 nm, "nanotext" and "nanologos".*

Figure A.10: *Photograph of OVD11 under two different viewing angles. It is a BrandMax OVD taken from [30] (Figure A.9) that consists of multiple optical effects, including 3D images.*

Figure A.11: *Photograph of OVD12 under three different viewing angles. It is a Chromagram from [30] (Figure A.15.I); the embossed diffractive surface is coated with an interference filter and pressed onto paper. The combination gives it a glossy metallic appearance.*

Figure A.12: *Photograph of OVD13 under three different viewing angles. It is a Chromagram taken from [30] (Figure A.15.II). The paper is coated with Optically Variable Adhesive (OVA), which gives it a matte metallic appearance.*

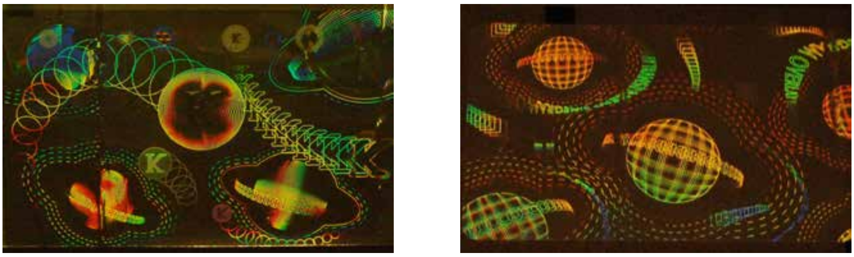

Figure A.13: *Photograph of (left) OVD14 and (right) OVD15. Both are embossed transmissive hologram foils.*

Figure A.14: *Photograph of OVD16, an embossed reflective hologram foil, under two different viewing angles.*

Bibliography

[1] F. Nicodemus, J. Richmond, J. Hsia, I. Ginsberg, and T. Limperis, *Geometrical Considerations and Nomenclature for Reflectance* (National Bureau of Standards, 1977).

[2] "Standard practice for Goniometric Optical Scatter Measurements, Tech. Rep.," *ASTM E2387–05 (American Society for Testing and Materials)* (2011).

[3] G. Obein, R. Bousquet, and M. E. Nadal, "New NIST reference goniospectrometer," Proc. SPIE 5880, 58800T-58800T-10 (2005).

[4] J. Suomalainen, T. Hakala, J. Peltoniemi, and E. Puttonen, "Polarised Multiangular Reflectance Measurements Using the Finnish Geodetic Institute Field Goniospectrometer," *Sensors* 3891-3907 (2009).

[5] L. Simonot and G. Obein, "Geometrical considerations in analyzing isotropic or anisotropic surface reflections," *Appl. Opt.* **46,** 2615–2623 (2007).

[6] V. B. Podobedov, M. E. Nadal, and C. C. Miller, "Improving the performance of NIST five axis goniospectrometer for measurements of bidirectional reflectance distribution function," Proc. SPIE, 806511 (2011).

[7] A. M. Rabal, A. Ferrero, J. Campos, J. L. Fontecha, A. Pons, A. M. Rubiño, and A. Corróns, "Automatic goniospectrophotometer for the absolute measurement of the spectral BRDF at in- and out-of-plane and retroreflection geometries," *Metrologia* **49,** 213 (2012).

[8] G. Obein, T. R. Leroux, and F. Vienot, "Bidirectional reflectance distribution factor and gloss scales," Proc. SPIE 4299, 279-290 (2001).

[9] L. Simonot, M. Hébert, and D. Dupraz, "Goniocolorimetry: From measurement to representation in the CIELAB color space," *Color Research & Application* **36,** 169–178 (2011).

[10] A. Höpe and K.-O. Hauer, "Three-dimensional appearance characterization of diffuse standard reflection materials," *Metrologia* **47,** 295 (2010).

[11] A. Ferrero, A. M. Rabal, J. Campos, A. Pons, and M. L. Hernanz, "Spectral and geometrical variation of the bidirectional reflectance distribution function of diffuse reflectance standards," *Appl. Opt.* **51,** 8535–8540 (2012).

[12] N. Johansson, *Measuring and modelling light scattering in paper*, PhD thesis (Mid Sweden University, 2015).

[13] G. J. Ward, "Measuring and Modeling Anisotropic Reflection," *SIGGRAPH Comput. Graph.* **26,** 265–272 (1992).

[14] J. R. Shell, "Bidirectional Reflectance: An Overview with Remote Sensing Applications & Measurement Recommendations," *Rochester Institute of Technology* (2004).

[15] J. F. Murray-Coleman and A. M. Smith, "The automated measurement of BRDFs and their application to luminaire modelling," *Journal of the Illuminating Engineering Society* (1990).

[16] A. Takagi, S. Sato, and G. Baba, "Prediction of spectral reflectance factor distribution of color-shift paint finishes," *Color Research & Application* **32,** 378–387 (2007).

[17] H. J. A. Saris, R. J. B. Gottenbos, and H. Van Houwelingen, "Correlation between visual and instrumental colour differences of metallic paint films," *Color Research & Application* **15,** 200–205 (1990).

[18] "Standard practice for specifying the geometry of multiangle spectrophotometers, Tech. Rep.," *ASTM E2194.01 (American Society for Testing and Materials)* (2001).

[19] "Tolerances for automotive paint - Part 2: goniochromatic paints," *Tech. Rep. DIN-6175-2 (Deutsches Institut für Normung)* (1999).

[20] A. Takagi, A. Watanabe, and G. Baba, "Prediction of spectral reflectance factor distribution of automotive paint finishes," *Color Research & Application* **30,** 275–282 (2005).

[21] E. Perales, E. Chorro, W. R. Cramer, and F. M. Martínez-Verdú, "Analysis of the colorimetric properties of goniochromatic colors using the MacAdam limits under different light sources," *Appl. Opt.* **50,** 5271–5278 (2011).

[22] W. R. Cramer, "Examples of interference and the color pigment mixtures green with red and red with green," *Color Research & Application* **27,** 276–281 (2002).

[23] E. Kirchner and W. Cramer, "Making sense of measurement geometries for multi-angle spectrophotometers," *Color Research & Application* **37,** 186–198 (2012).

[24] A. Ferrero, A. M. Rabal, J. Campos, A. Pons, and M. L. Hernanz, "Variables separation of the spectral BRDF for better understanding color variation in special effect pigment coatings," *J. Opt. Soc. Am. A* **29,** 842–847 (2012).

[25] "Multimedia systems and equipment – color measurement and management: Part 2-1. Color management–default RGB color space – sRGB," *IEC 61966-2-1* (1999).

[26] J. K. Nisper, P. S. Rood, B. A. Pawlanta, T. M. Richardson, and B. D. Teunis, "Measuring An Appearance Property Of A Surface Using A Bidirectional Reflectance Distribution Function," *U.S. Patent 2007/0291993 A1* (20 December 2007).

[27] J. K. Nisper, T. M. Richardson, M. S. Ellens, and C. Huang, "Method And System For Enhanced Formulation And Visualization Rendering," *U.S. Patent 2009/0213120 A1* (27 August 2009).

[28] T. R. J. Nisper and B. Teunis, "Major advances in the reliable measurement of the color and appearance of special effect paints and coatings," *presented at the American Coatings Conference, Charlotte, North Carolina* (1 April 2008).

[29] J. Goodman, *Introduction to Fourier Optics*, 2nd ed. (McGraw-Hill, 1996).

[30] R. L. van Renesse, *Optical Document Security, 3rd edition* (Artech House, Boston/London, 2005).

[31] L. Kotačka, T. Têthal, and V. Kolařik, "Top-quality security optical elements: from holography towards 500.000 dpi," Proc. SPIE 5954, 59540K-59540K-9 (2005).

[32] A. Argoitia and R. Phillips, "The security enhancement of diffractive optically variable image devices," Proc. SPIE 6075, 60750P-60750P-18 (2006).

[33] S. Sumriddetchkajorn and Y. Intaravanne, "Hyperspectral imaging-based credit card verifier structure with adaptive learning," *Appl. Opt.* **47,** 6594–6600 (2008).

[34] S. Sumriddetchkajorn and Y. Intaravanne, "Data-nonintrusive photonics-based credit card verifier with a low false rejection rate," *Appl. Opt.* **49,** 764–771 (2010).

[35] E. Faulkner and R.J.Schwartz, *High Performance Pigments*, 2 ed. (Wiley-VCH, 2009).

[36] P. Wissling, *Metallic Effect Pigments: Basics and Applications*, 1 ed. (Vincentz, 2006).

[37] G. Pfaff and P. Reynders, "Angle-Dependent Optical Effects Deriving from Submicron Structures of Films and Pigments," *Chemical Reviews* **99,** 1963–1982 (1999).

[38] F. J. Maile, G. Pfaff, and P. Reynders, "Effect pigments–past, present and future," *Progress in Organic Coatings* **54,** 150 – 163 (2005).

[39] E. Kirchner and J. Houweling, "Measuring flake orientation for metallic coatings," *Progress in Organic Coatings* **64,** 287 – 293 (2009), Coatings Science International 2008.

[40] T. Germer and M. Nadal, "Modeling the appearance of special effect pigment coatings," Proc. SPIE 4447, 77-86 (2001).

[41] T. Germer, J. Zwinkels, and B. Tsai, *Accurate Measurement of Optical Properties of Materials (Experimental Methods in the Physical Sciences)*, Vol. 46, 1 ed. (Academic Press, 2014).

[42] M. Klanjšek Gunde, M. Kunaver, M. Mozetič, P. Pelicon, J. Simčič, M. Budnar, and M. Bele, "Microstructure analysis of metal-effect coatings," *Surf. coat. int., Part B, Coat. trans.* **85,** 115–121 (2002).

[43] F. Schmollgruber, "xDNA: What can new Color evaluation concepts do for us," *internal document, presentation in Helios factory (Slovenia)* (April 2012).

[44] E. Hecht, *Optics*, 4 ed. (Addison-Wesley, 2001).

[45] K. E. Torrance and E. M. Sparrow, "Theory for Off-Specular Reflection From Roughened Surfaces," *J. Opt. Soc. Am.* **57,** 1105–1112 (1967).

[46] E. Palik, *Handbook of Optical Constants of Solids* (Academic Press, 2002).

[47] S. N. Kasarova, N. G. Sultanova, C. D. Ivanov, and I. D. Nikolov, "Analysis of the dispersion of optical plastic materials," *Optical Materials* **29,** 1481 – 1490 (2007).

[48] "Database of Optical Constants for Cosmic Dust," *Laboratory Astrophysics Group, University of Jena, Germany, (available at: <http://www.astro.uni-jena.de/Laboratory/OCDB/>)* (Accessed 10 August 2015).

[49] A. Argoitia and S. Chu, "Diffractive pigments help document security," *European Coatings Journal* (2004).

ERRATA

- p. 39
  Equation 4.27(c) should read $\mu^z = \cos\varphi_{as}$
- The Equation 4.27(c) was used as it is printed in the thesis for the calculations of the xDNA curves for some of the examples in the section 5, therefore the following visuals are not entirely correct (the z axis is wrong):
  Subsection 5.2: Figures 5.5–5.10, sub-figures (b) of Figures 5.11–5.22
  Subsection 5.3: Figures 5.23–5.25, 5.26 (c) and (d), 5.27–30, 5.31 (d) and (e), sub-figures (c) of Figures 5.32–5.36, and sub-figures (b) of Figures 5.37–5.52.
  Shown below are a few corrected figures. One can see, that the effect of the error is relatively small and that the conclusions derived from the figures still stand.
- p. 52, Figure 5.8
  The legend in both sub-figures should be corrected. It should read "black line–3, red line–2 and green line–1.
- p. 53, Figure 5.10
  The mark in the sub-figure (a) for the black xDNA curve should read G10, instead of G6.
- p. 4, second paragraph, second sentence
  There is an extra "in most cases" in the sentence. It should be "In most cases, the data are represented as a matrix ...".
- List of publications
  Paper VI has been accepted for publishing since the printing of the thesis began.
- The already accepted and published Papers II and VI will receive an errata to correct for the mistakes made because of the Equation 4.27(c), and the still submitted Paper IV will be corrected before publishing.

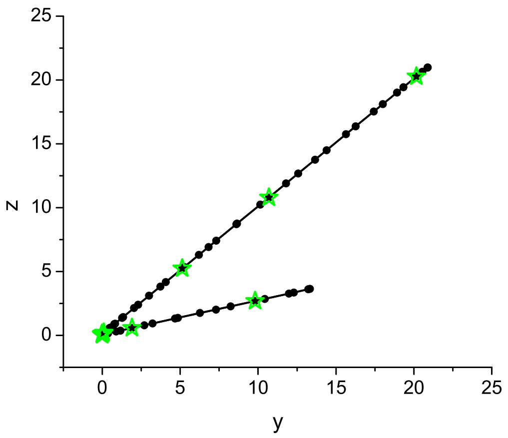

Corrected Figure 5.5, page 49.

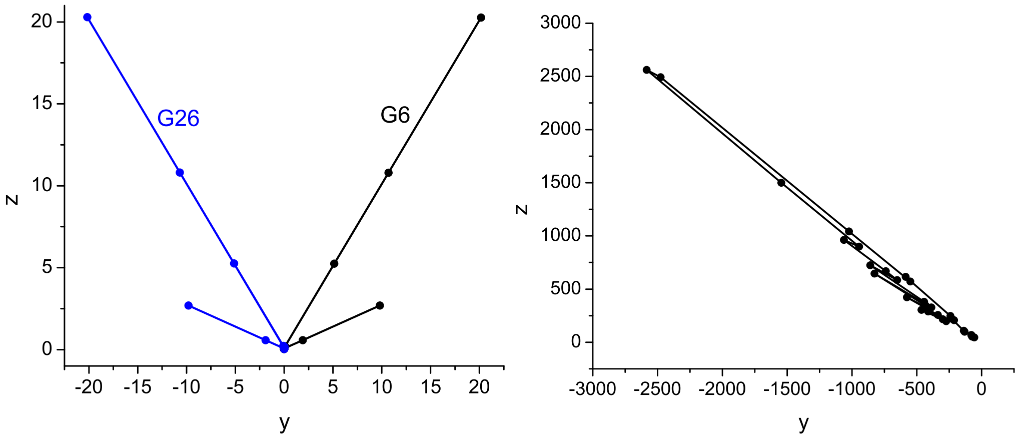

(a) (b)

Corrected Figure 5.9, page 52

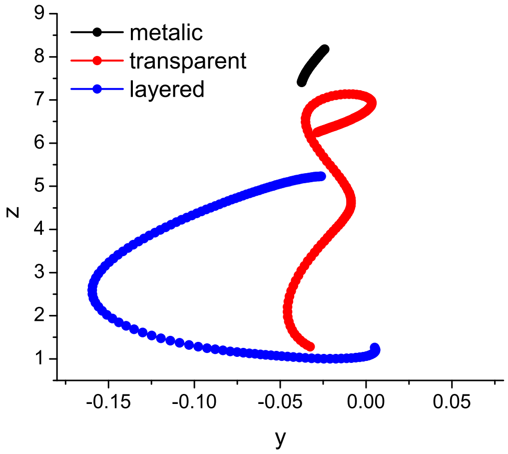

Corrected Figure 5.23, page 60

Nina Rogelj

Goniospectrometric analysis of optically complex samples

A study of diffraction gratings, optically variable devices, and coatings with special effect pigments

This study focuses on how to characterize gonioapparent targets, whose appearance depends on illumination and viewing angles, by using a transformation of the BRDF to goniospectrometric space. A systematic analysis of the method is performed for optically complex samples. It is shown that measurement geometry using 10 reflected angles at a 45° illumination angle with reduced spectral resolution is suitable to obtain a unique xDNA curve that truly characterizes the optically complex sample.

UNIVERSITY OF
EASTERN FINLAND

Publications of the University of Eastern Finland
Dissertations in Forestry and Natural Sciences

isbn: 978-952-61-1986-1 (printed)
issn: 1798-5668
isbn: 978-952-61-1987-8 (pdf)
issn: 1798-5676